Comments on Inorganic Chemistry
Publication details, including instructions for authors and subscription information:
http://www.informaworld.com/smpp/title~content=t713455155

Integrated Optics: A New Focus for Inorganic Chemistry

Dehipawalage Sunil; P. Sujatha Devi; Jinquan Dong; Arthur W. McQuade; Edgar A. Mendoza; Harry D. Gafney

Online publication date: 24 June 2010

To cite this Article Sunil, Dehipawalage , Devi, P. Sujatha , Dong, Jinquan , McQuade, Arthur W. , Mendoza, Edgar A. and Gafney, Harry D.(2003) 'Integrated Optics: A New Focus for Inorganic Chemistry', Comments on Inorganic Chemistry, 24: 3, 69 — 136
To link to this Article: DOI: 10.1080/714912227
URL: http://dx.doi.org/10.1080/714912227

Comments on Inorganic Chemistry, 24: 69–136, 2003

ISSN: 0260-3594 print
DOI: 10.1080/02603590390228137

Taylor & Francis
Taylor & Francis Group

Integrated Optics: A New Focus for Inorganic Chemistry

Dehipawalage Sunil, P. Sujatha Devi, Jinquan Dong, Arthur W. McQuade, Edgar A. Mendoza and Harry D. Gafney*
Department of Chemistry, City University of New York, Queens College, Flushing, NY 11367, USA

Photopatterning metal and/or metal oxides in porous, silica-based glasses and xerogels followed by thermal consolidation to a nonporous glass yields refractive index gradients that, depending on their shape, guide, focus, and defract light. The optical performance of these structures depends on the species photodeposited in the matrix, the changes they undergo during consolidation of the matrix, and their effect on the consolidating matrix. Gradient index structures derived from $Fe(CO)_5$ are composed of nanometer diameter metal and/or metal oxide particles, whereas those derived from $(CH_3)_3SnI$ are composed of individual oxides or smaller aggregates within the SiO_2 matrix. Porous Vycor glass acts as a template for Fe^o-Fe_2O_3 particle growth during consolidation with the resulting gradient index structure consisting of 10 ± 1 nm diameter particles composed of small aggregates of elemental iron dispersed in Fe_2O_3 with an average inter-particle spacing equivalent to the correlation length of the porous glass. Consolidation of the xerogel produces equivalent changes in refractive index and similar changes in the electronic spectra, but the gradient index is composed of a mixture of octahedrally and tetrahedrally coordinated Fe^{3+} present as individual molecular species, or as ≤ 1-nm diameter aggregates incorporated into the silica network. Photodeposition of tin offers a means to pattern porosity within a consolidated glass and a means to incorporate reagents unable to withstand the consolidation temperature of glass. Pattern resolution is limited by scattering of the photolyzing light by the SiO_2 nodules of the porous matrices, but thermal consolidation of the matrices occurs without loss of pattern resolution. Consistent with a random distribution of pores throughout these silica

*Corresponding author

matrices, the change in pattern dimension on consolidation can be calculated from the void volume of the matrix. Various optical structures created by these photodeposition techniques and their optical performance are described.

INTRODUCTION

Photonics, a word derived from photon and electronics, defines an area of investigation and application that exploits the extraordinary coherence, power, monochromaticity and time resolution of cw and pulsed lasers to develop optical analogues of electronic devices and circuits. Like any circuit, photonic circuits consist of active and passive elements. Passive elements, analogous to wires and printed circuit boards, guide the light between the different active elements that, like transistors, capacitors, rectifiers, and resistors, modify the frequency, phase, and coherence of the photons passing through the circuit.[1,2] Many optical circuits currently exist, but in most cases, these are large collections of lenses, mirrors, beam splitters, and magneto- and/or electro-optical devices dispersed on optical benches. Integrated optics addresses the practical need to miniaturize these complex, multi-component systems and incorporate the active and passive elements in a single medium.

Photonic systems for telecommunications or optical signal processing, for example, will integrate lasers, waveguides, couplers, switches, optical detectors, and "smart" sensors.[3–8] These optical components are currently realized in diverse materials including compound semiconductors, inorganic crystals, glasses, and various electro-optic, magneto-optic, and piezoelectric materials. Two concerns are the ability to economically integrate these components and the ability to avoid the degradation in reliability and performance associated with the interfaces between dissimilar components. If an economical and resilient material can be found that allows the incorporation and ready connection of compatible optical components, however, the cost of integration declines and the ability to innovate complex circuitry increases. Such a material, which offers compatibility at the material and device level, is often referred to as "optical silicon." Here, we show that porous glasses and sol-gel–derived porous xerogels offer many of the advantages required of "optical silicon," and that deposition of metals and metal oxides in these substrates is a promising, but challenging, approach to integrated optics.[9–15]

Glass is an excellent, inexpensive material in which to integrate active and passive optical elements. It is moldable and stable under a variety of conditions, transparent to wide range of wavelengths, compatible with fiber-optic technology, and tolerant of high input powers. This is a specific advantage if high laser powers are to be exploited to achieve nonlinear optical phenomena.[5,8] On the other hand, glass is a refractory, and its processing temperatures, typically greater than 1000°C, present a challenge with respect to integrating active and passive components into the medium, and coupling

these "optical chips" into a coherent network. We believe inorganic chemistry will play a pivotal role in developing integrated optics, not because of a presently known optical or spectroscopic property. In fact, currently available organic polymers offer a number of advantages with respect to synthesis, tailoring and tuning specific optical properties, and assembly into compact structures. Rather, our belief stems from the simple idea that most metals and metal oxides are capable of withstanding the processing temperatures of glass,[16] and dispersed in a glass matrix, capable of withstanding high incident laser intensities. Sol-gels, sol-gel–derived porous xerogels,[17] and acid-leached porous glasses[18] such as Corning's code 7930 porous Vycor glass (PVG) can be impregnated under less demanding conditions and, therefore, with a wider variety of reagents. However, practicality demands either filling the pore structure with a refractive index matching material, encapsulating the porous substrate, or consolidating the matrix to a nonporous, nonscattering glass.[16] At this point, it is not clear which is the best approach, and it is quite possible that viable systems will be a hybrid of all.

Analogies to integrated electronic circuits often accompany discussions of integrated optics, but a fundamental difference germane to the choice of substrate and the creation of the optical elements must be recognized. Electrical conduction occurs principally on the surface of the conductor, and many electronic devices are layered structures whose performance is dictated, to a large extent, by the sharpness of the interface. Optical conduction, on the other hand, occurs in the bulk of the conductor. Doping to achieve a specific optical property therefore must be in the bulk, and, to minimize scattering losses, uniformly throughout the optical pathway. Moreover, the dopant will have to be patterned to achieve the desired optical property, or high element density per unit volume.[13,19] Maximizing element density is not necessarily to achieve faster operation, but to minimize optical losses. Since many integrated optical devices will consist of different materials in a common substrate, minimizing light losses by reducing the distance the light travels and the number of scattering centers it encounters within the device is crucial. Without adequate consideration at the materials development stage, subsequent scattering losses and lower transmissivity quickly become inherent limitations.

As noted, patterning is crucial to achieving many optical properties. The ability to guide light within a medium rests on the *difference* in refractive index between the guiding structure, called the core, and its surroundings, called the cladding, i.e., its direction of propagation changes when light encounters a change in refractive index.[13,20–24] The difference in refractive index defines the critical angle, θ_c,

$$\sin \theta_c = n_{cl}/n_{cr} \qquad [1]$$

where n_{cr} is the refractive index of the core and n_{cl} is that of the cladding. For a cylindrical optical fiber, the critical angle defines a cone of propagation so that light entering the core within this cone satisfies the condition for internal

reflection and propagation through the optical fiber. In a miniaturized optical circuit, the passive component, referred to as a waveguide, performs the same function as the core of the optical fiber and is subject to the same principles governing propagation in a fiber. The reader is referred to a number of excellent references describing optical transmission with the caution that, because optical propagation depends on the shape of the conductor, the equations contain different geometrical parameters.[20–23] Unlike an optical fiber, where a cladding of lower refractive index is deposited on a core of higher refractive index,[24] in integrated optics the medium, in this case the glass host, is the cladding, and the problem becomes one of patterning a core, i.e., a well-defined volume of higher refractive index.[13]

The refractive index, n, of homogeneous isotropic matter is a function of its density, ρ, and its mean optical polarizability, α,

$$(n^2 - 1)/(n^2 + 2) = 4\pi\alpha N_o\rho/3M \qquad [2]$$

N_o is Avogadro's number and M is the molar mass of the material.[20–23,25,26] Assuming average density and polarizability, since structures created by photodeposition are not necessarily homogeneous or isotropic, incorporating a material that increases either the average density or mean optical polarizability of a specific volume increases the average refractive index of that volume relative to that of the bulk. The derivative of refractive index with respect to density, $dn/d\rho$, is positive, implying Δn increases in proportion to the amount deposited. The situation is more complex with respect to molar polarizability. Nevertheless, provided the ratio of polarizability to partial molar volume of the dopant exceeds that of the host matrix, refractive index increases in proportion to the amount deposited.

In a classic series of experiments, Borrelli, Morse and their coworkers showed that the photodegradation of organometallics adsorbed onto Corning's code 7930 porous Vycor glass (PVG) increases the refractive index of the glass.[27–29,30] Subsequent experiments confirm changes in refractive index at 632 nm ranging from 10^{-6} to 0.67 in PVG[31] and porous glasses derived from the base-catalyzed condensation of tetramethylorthosilicate, ethanol, and water ($TMOS/EtOH/H_2O$).[32] The upper limit is simply an experimental limit imposed by a loss of transparency at the measuring wavelength. Regardless of the Δn achieved, the striking and perhaps more important result is that both PVG and the xerogel can be consolidated to a nonporous glass without loss of pattern resolution.[32] Consolidation of these materials, which are composed of silica nodules with the intervening spaces defining a random array of interconnected pores throughout the matrix[17,32] is essential to minimize scattering. Consolidation is not a single process occurring at a specific temperature, but a sequence of steps, which ultimately reduces the sample volume by 30–40%.[13,32] Nevertheless, these materials can be consolidated to a nonporous, nonscattering glass without loss of pattern resolution.[32] In fact, in applications described below, the

reduction in volume accompanying consolidation becomes a design parameter exploited to improve optical performance.

Work in this laboratory focuses on characterizing the mechanism by which the complex adsorbs onto the glass, the photophysics and photochemistry of the adsorbed complex, and the photoproducts formed in these matrices.[33–35] Deposition to achieve optical performance, however, quickly broadens the experimental vista to include parameters such as precursor diffusion, photoproduct distribution and aggregation, the changes the photoproducts undergo during matrix consolidation, and their effect on the matrix itself.[36–40] This discussion focuses on gradient indices derived from the photolysis of $Fe(CO)_5$[32,33] and $(CH_3)_3SnI$[34,35] adsorbed into Corning's code 7930 porous Vycor glass and porous xerogels derived from the base-catalyzed condensation of alkoxysilanes.[17] Specifically, the adsorption and photochemistry of these precursors are described as well as the changes the photoproducts undergo during consolidation of the silica matrices, their distribution and aggregation within these matrices, and their effect on the host matrix.[37–39] With the current emphasis on the nanometer domain, it is important to realize that deposition of an optical structure spans dimensions ranging from nanometers to microns. Structures capable of diffracting light, for example, may span tens to hundreds of microns, whereas the transmissivity and transparency of a waveguide may reflect the nature and size of the species deposited to create the refractive index gradient. To illustrate the point, a number of optical structures created with these precursors and their optical performance are described. Although we believe porous glasses and xerogels satisfy many of the criteria of "optical silicon," the quoted optical performance parameters will fail to convey that impression. It is therefore important to point out that no attempt has been made to optimize the deposition procedure to a specific optical application, or to maximize the coupling between the probe light used to measure optical performance, usually an He-Ne laser, and the structure. The transmissivity of a waveguide, for example, is taken simply as the ratio of power transmitted relative to the output of the He-Ne probe laser. Nevertheless, it gives the reader an idea of performance achieved under rudimentary deposition procedures, and more importantly, may spur new ideas to improve optical performance.

Porous Glass and Xerogels

Xerogels and Corning's code 7930 porous Vycor glass are chemically and morphologically similar materials but are obtained by completely different methods.[17,41] Derived from a 96% SiO_2, 3% B_2O_3 and 1% Na_2O and Al_2O_3 melt, PVG is formally a glass, i.e., it has been heated beyond its sintering temperature. However, the melt phase separates on cooling, and acid leaching removes the borate phase, leaving a transparent material (50%T at 350 nm) that consists of silica nodules with the spaces between the nodules

defining an array of interconnected pores randomly dispersed throughout the material.[43] Although the silica nodules are on the order of 3–5 μm in diameter (Figure 1), they define a surprisingly narrow range of pore diameters, 10 ± 1 nm.[13,32] Higher resolution AFM analysis reveals another level of structure on the nodule surfaces (Figure 2) that appear as sharp stalagmites on the order of 25 ± 5-nm wide and 25 ± 5-nm high on the surface of the 3–5 μm diameter silica nodules. The dimensions of these structural elements are equivalent to the correlation length of the glass obtained from small

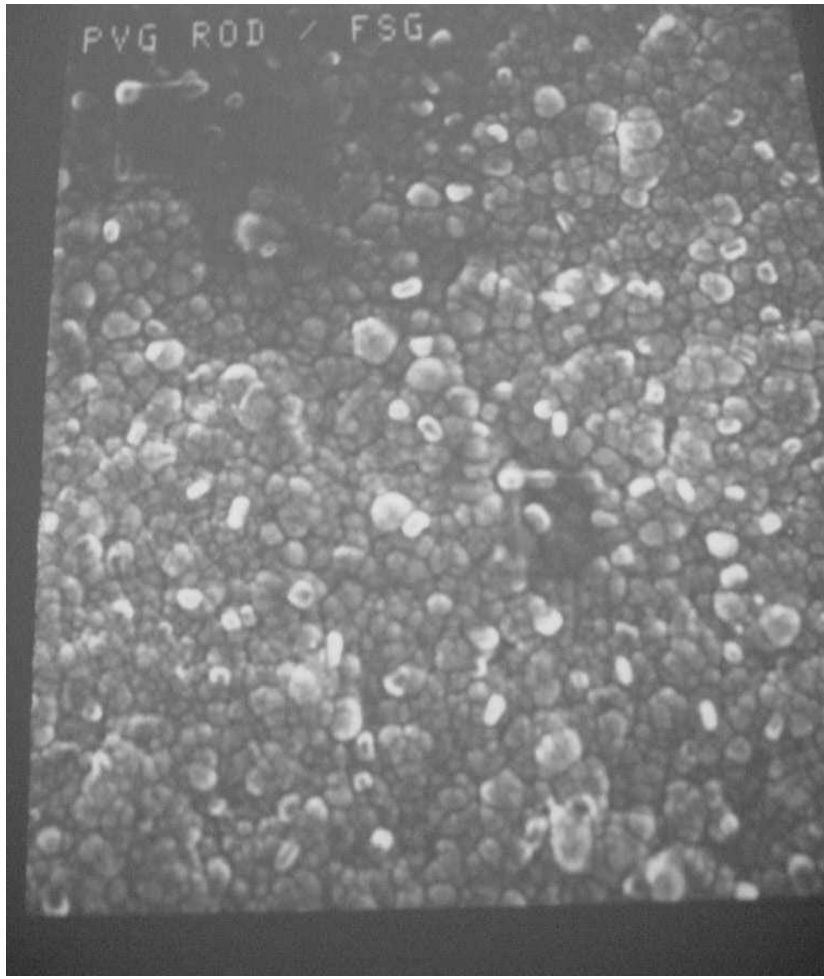

FIGURE 1 SEM of polished PVG dried at 600°C.

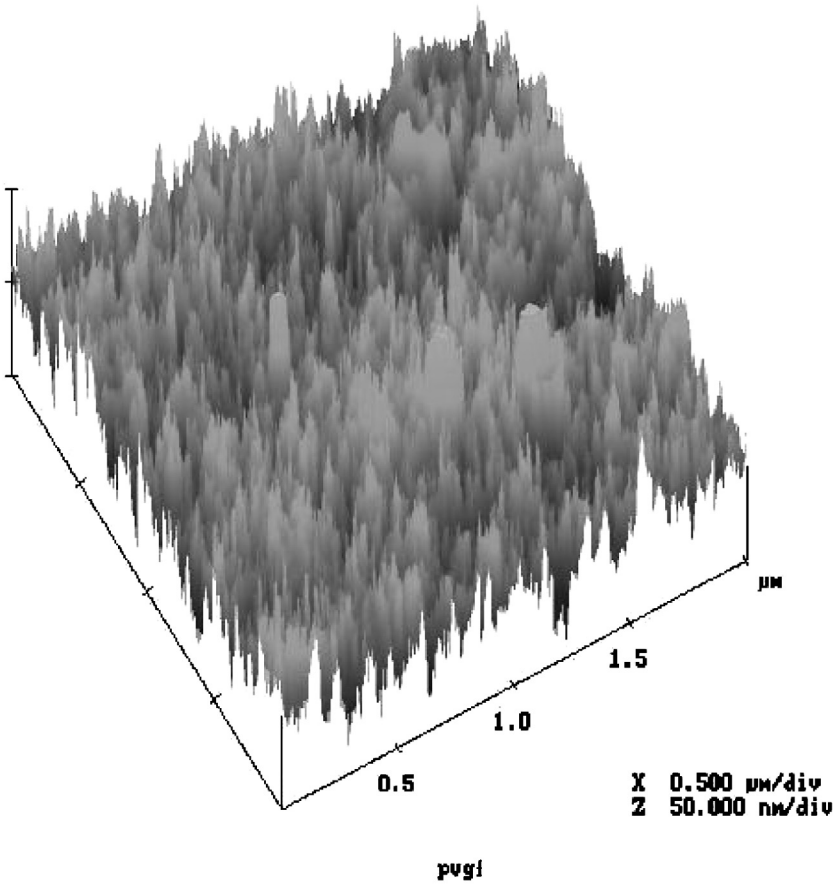

FIGURE 2 AFM of polished PVG dried at 600°C.

angle X-ray (SAXS) and neutron scattering (SANS), 22 ± 1 nm,[38,46] implying that these are the finest structural features of PVG.[48]

TMOS/MeOH/H_2O and TEOS/EtOH/H_2O xerogels are prepared by the base-catalyzed (NH_3) gellation of tetramethoxysilane, methanol, and water, or tetraethoxysilane, ethanol, and water.[17] These materials are gelled at room temperature and then slowly dried at room temperature. Slow drying over a period of days to weeks is crucial to obtaining a transparent, solid, glass-like material. Attempts to speed this step up either by drying under vacuum at room temperature or drying at higher temperatures simply promotes cracking and the sample breaks up.[47] Depending on the application or experiments, some samples were used after drying at room temperature, while

others were then slowly ($\leq 0.5°C$/minute) heated to 500°C, maintained at this temperature for 24 hours, and then slowly ($\leq 2°C$/minute) cooled to room temperature. Regardless of the drying procedure used, the resulting samples, which are referred to as an xerogel, have the physical appearance of glass, but since they have not been heated to the sintering temperature, $\geq 800°C$, they are not formally a glass. Nevertheless, the xerogel is chemically and structurally similar to PVG, and both materials, when heated to temperatures $\geq 1000°C$, consolidate to a nonporous SiO_2 glass.

TMOS/MeOH/H_2O and TEOS/EtOH/H_2O xerogels, whether dried at room temperature or dried at 500°C, possess a structural motif composed of silica nodules with the intervening spaces defining a pore structure randomly dispersed throughout the material (Figure 3).[48] The silica nodules making up the xerogel (Figure 3) range from 2 to 4 μm in diameter. In contrast to PVG, however, the structural features on the silica nodules are much smaller. Even at six times higher resolution in the plane of the surface and twice the resolution perpendicular to the xerogel surface, the structural features evident across the entire PVG surface (Figure 4) are apparent only along the edges of the AFM image of the xerogel surface.[48] The features on the xerogel, 1–3 nm in width and 1–2 nm high, are about an order of magnitude smaller than those found on PVG (Figure 2). In spite of their macroscopic appearance, which suggests that PVG is a more uniform material, on the nanometer length scale the surfaces of the xerogel are much smoother than those of PVG. The irregularity of the xerogel surface, i.e., the deviation from a hypothetical flat surface, is ± 286 nm, while that of the PVG surface is ± 440 nm.[48] These numbers are much larger than the structural features on the surface of the silica nodules because, measured over distances of microns on the surface of each matrix, the irregularity of the surfaces reflects the openings into the interior pore structure. Although the surface of PVG is more irregular, N_2 desorption yields a narrow range of 10 ± 1 nm diameter pores.[32] In contrast, N_2 desorption from xerogels heated to 500°C, which possess smoother interior surfaces, yields pore diameters ranging from 0.5 nm to 1–2 μm. Also, the measured surface area of PVG, $183 \pm 15\ m^2/g$ at 25°C, is smaller than that of the heated xerogel, $508 \pm 18\ m^2/g$ at 25°C. Apparently, the surface areas of these materials reflect the larger structural features, such as pore diameter, rather than the smaller, nanometer-sized features present on the surfaces of the silica nodules. Both measurements, however, are based on N_2 adsorption with the surface area calculated from the amount of N_2 adsorbed/g of material, and the average pore diameters calculated from its desorption via the Kelvin equation. Although well established, widely used, accepted methods,[49] which use a nonpolar adsorbent, N_2, much smaller than any of the above structural features (the N-N bond length is 0.1 nm[50]), the smaller surface area of PVG, when compared to the larger structural features revealed by AFM, leads one to wonder about the reliability of the N_2 adsorption-desorption measurements.

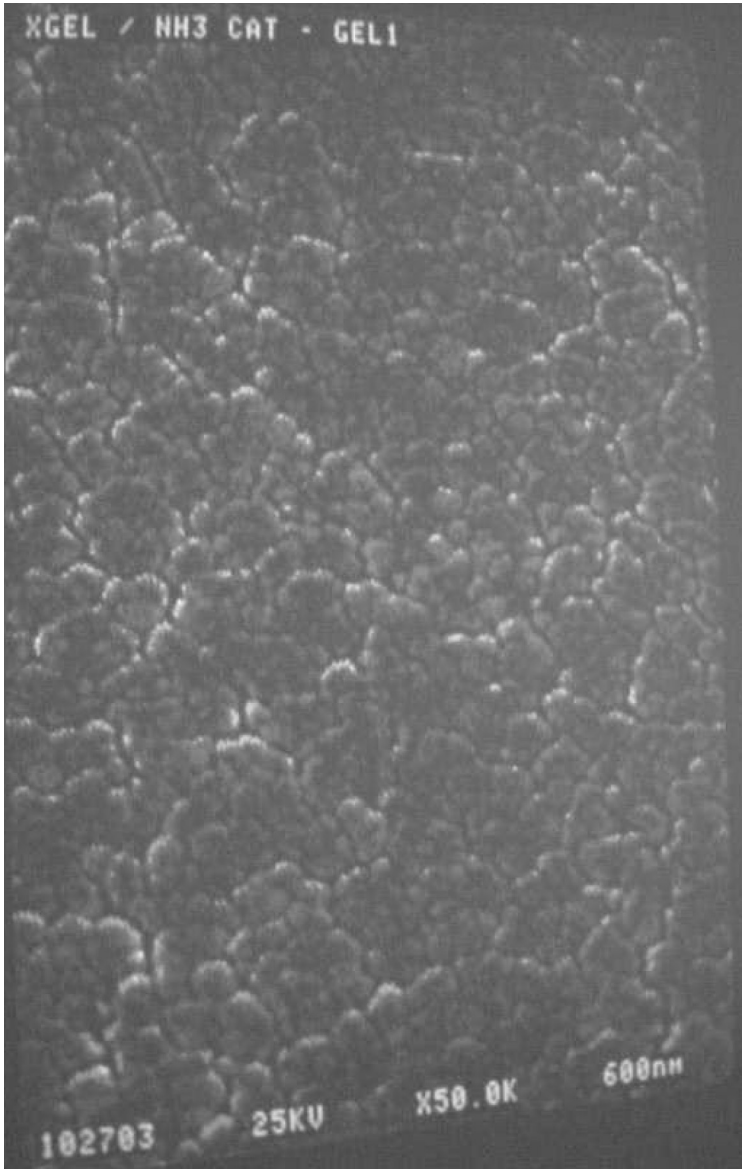

FIGURE 3 SEM of base-catalyzed TMOS/MeOH/H_2O xerogel dried at 650°C.

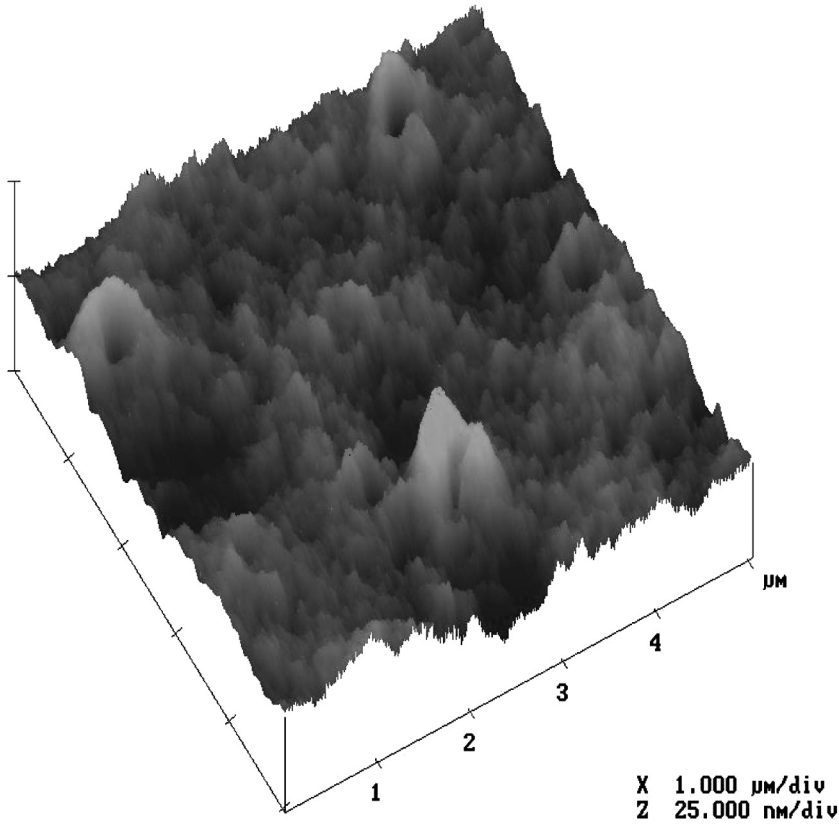

FIGURE 4 AFM of base-catalyzed TMOS/MeOH/H_2O xerogel dried at 650°C.

Although differing in the size of the surface structures, both materials possess Si-OH surface functionalities present as either individual silanols, called free silanols, or groups of hydrogen-bonded silanols called associated silanols.[44,45] The free silanols are characterized by an intense band in the region of 3750 cm^{-1}, while the associated silanols are characterized by a band in the 3650 cm^{-1} region that usually appears as a shoulder on the more intense 3750 cm^{-1} band. Both types of silanols are present in both materials, although the number of silanol groups/unit area, the silanol number, has not been quantitated for PVG or these xerogels. The silanol number depends on the thermal history of the sample, and previous studies of dried silicas yield a silanol number of 4–7 Si-OH groups/10 nm^2.[51] The average of 5 Si-OH groups/10 nm^2 correlates well with the chemistry of the sub-carbonyls produced by photolysis of $W(CO)_6$ physisorbed onto PVG and is assumed to be the silanol number of both materials.[52,53]

Heating either material collapses the pore structure and condenses the surface silanols to form an Si-O-Si glass, but the individual sequence of steps and the temperatures at which they occur differ in the two materials. Both materials begin to shrink with the desorption of physisorbed water around 100°C (Figure 5), but neither change is initially evident as a change in surface area.[47,48] The surface area of PVG shows little change up to 600°C, and then declines smoothly with the sharpest decline in the 900–1000°C region (Figure 6). At 650°C, the individual silica nodules begin to broaden and meld together with a concurrent decline in the intensity of the silanol vibrations at

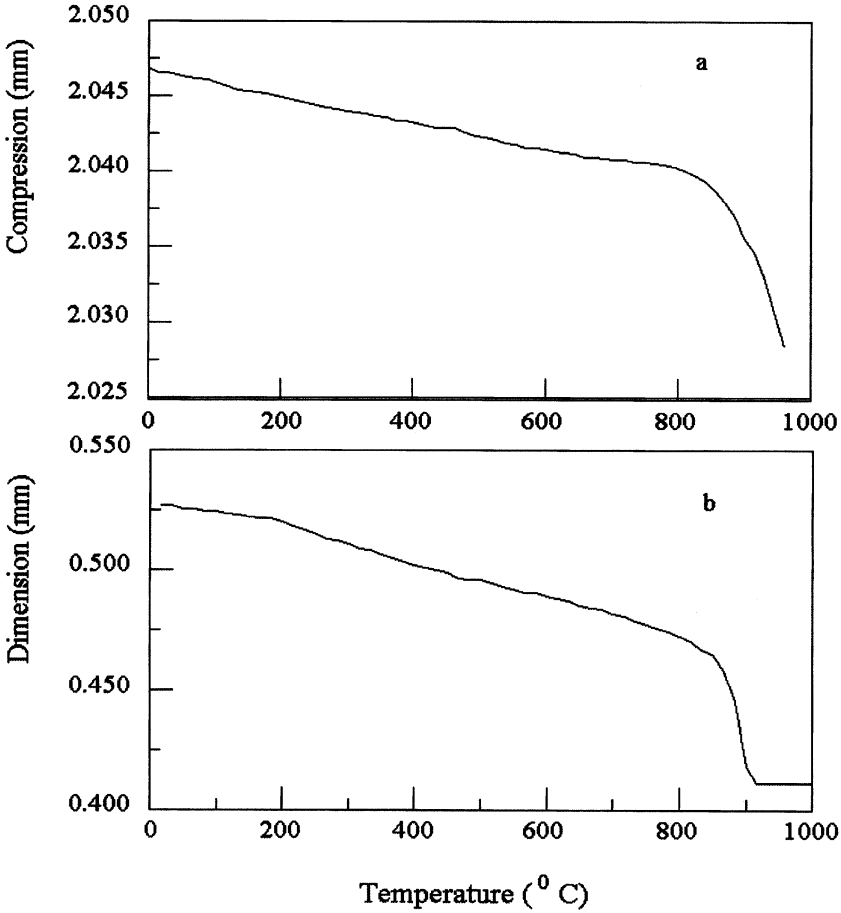

FIGURE 5 Thermomechanical analysis of (a) PVG and (b) TMOS/MeOH/H_2O xerogel.

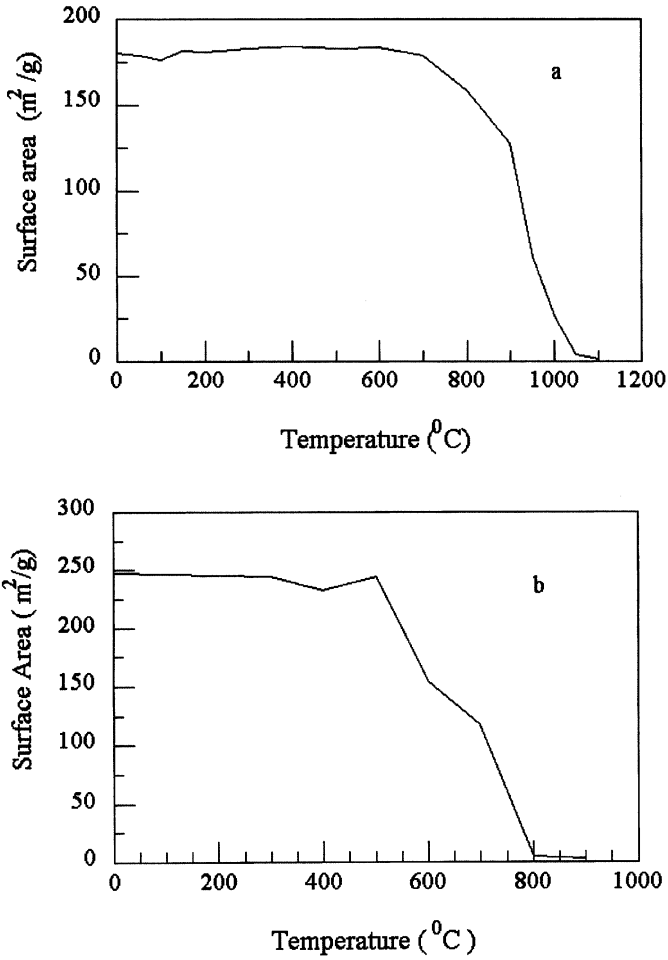

FIGURE 6 BET surface area of (a) PVG and (b) TMOS/MeOH/H_2O xerogel as functions of temperature.

3744 and 3655 cm^{-1} as the surface silanol groups condense to form Si-O-Si bonds. The surface area of the xerogel shows little change up to ca. 300°C, but then begins to oscillate, showing both increases and decreases prior to large decline in the 500 to 800°C range (Figure 6). The oscillations in surface area in the 300 to 500°C region correlate with exothermic processes at 380 and 440°C. The 380°C process is attributed to the decomposition of the organic components of the xerogel since it is accompanied by a decline in the intensity of the 2959 and 2852 cm^{-1} bands of Si-OCH_3[32] and the devel-

opment of a gray or gray-black color.[32] The 440°C process occurs with the loss of the gray or gray-black color and is assigned to the desorption of the decomposition products.[47,48] Decomposition and desorption of the organic constituents create a chaotic domain, where the interior and exterior surfaces of the xerogel are in a state of flux, showing both increases and decreases in surface area. In fact, a number of AFM images of the xerogels show sharp-edged craters (Figure 7) that appear to be caused by the gaseous decomposition products bursting out through the skinned-over surface of the xerogel. Cone-shaped structures visible in Figure 4 appear to be hollow and may also arise from the desorption of the organic constituents or their decomposition products, although in this case the structure has been smoothed by more extensive annealing. Derived from a melt devoid of organic components, this chaotic domain is not evident in the consolidation of PVG. Beyond this intermediate chaotic domain, however, consolidation of the xerogel parallels the consolidation of PVG.

Consolidation, which begins to occur at 500°C in the xerogel and 600°C in PVG, is not a single process involving conversion to a liquid phase, but a sintering, i.e., a sequence of steps beginning with the broadening of the

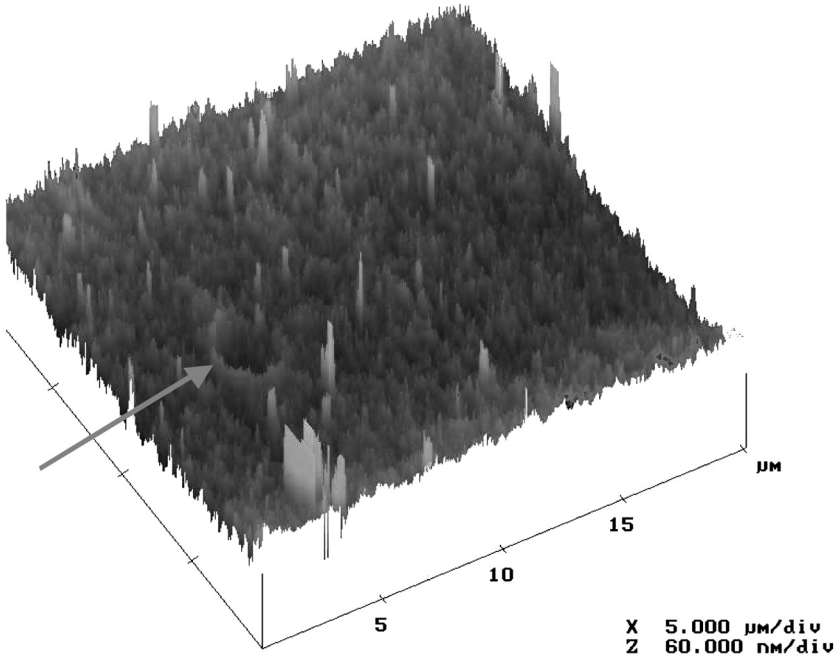

FIGURE 7 AFM image of a creator (arrow) attributed to the desorption of the organic components from a TMOS/MeOH/H_2O xerogel heated to 600°C.

silica nodules and their melding together to form nonporous glass.[54] A decline in the intensities of the free and associated silanol bands accompanies the melding of the nodules as the surface silanol groups condense to an Si-O-Si glass. The glass transition temperature in PVG occurs at $870 \pm 30°C$, and an exothermic process at $1105 \pm 18°C$ and spanning ca. 100°C is attributed to the release of surface energy due to viscous sintering.[32,47] Heating the xerogels leads to similar changes; the nodules broaden and meld together with an accompanying decline of first the 2959 and 2852 cm^{-1} methyl bands and then the SiO-H bands in the vicinity of 3750 and 3650 cm^{-1}.[32] A series of slightly exothermic process above 800°C points to similar structural relaxations accompanying the sintering of the xerogel.[47] Thus, heating either material to 1200°C leads to sintering and a fully consolidated, nonporous silica glass.

The Si-O bond energy, 185 kcal/mol, far exceeds most transition metal-oxygen bond energies.[55] For example, the Fe-O and Sn-O bond energies, which are the two metals this article focuses on, are only 92 kcal/mol and 132 kcal/mol, respectively.[55] As described below, there is no evidence of the formation of a metal-silicon bond. Consequently, at the sintering temperatures for PVG and these silica-based xerogels, there should be more than enough energy to break any metal-oxygen bond that might be formed between the photodeposited material and the matrix. Therefore, the ability to pattern a metal and/or a metal oxide in these refractories is not the result of bonding the photoproduct to the matrix. Instead, the photochemical reaction converts a volatile precursor to a less volatile metal and/or metal oxide, which is then entrapped between the melding silica nodules.[13,19] This suggests that the limit of pattern resolution is the dimension of the features on the silica nodule surfaces, or in the case of PVG, the correlation length of the glass, 22 ± 1 nm. We will return to the question of pattern resolution later on, but it is worthwhile to point out at this point that the limit of resolution accessible in these porous matrices is sufficient for all near-UV, visible, and near-IR optical structures.

Photodeposition in Porous Vycor Glass and Porous Xerogels

Photodeposition of an optical element in a porous glass or xerogel involves four steps: adsorption of a photoactive precursor into the porous matrix, the photochemical reaction, desorption of the unreacted precursor, and thermal consolidation of the matrix to a nonporous, nonscattering glass. As noted above, this discussion focuses on two precursors, $(CH_3)_3SnI$ and $Fe(CO)_5$. $Fe(CO)_5$ physisorbs onto PVG and the xerogel without disruption of its primary coordination sphere. The major CO bands of the adsorbed complex, designated $Fe(CO)_5$(ads), occur at 2004 and 2026 cm^{-1}. The band energies are slightly lower than those found in the vapor phase spectrum, 2012 and 2033 cm^{-1}, and the relative intensities are inverted relative to the vapor

phase spectrum.[33] In the vapor phase, the lower wave number band is the most intense, whereas the higher wave number band is most intense in the adsorbed complex. The change in the relative intensities as well as the appearance of a weak $2114\,cm^{-1}$ band suggest the complex distorts on adsorption,[57] but this does not significantly change in electron density or distribution at the metal center. The isomer shift and quadrupole splitting of the adsorbed complex are equivalent to those of neat $Fe(CO)_5$, $-0.087 mm/s$ and $2.57\,mm/s$, respectively, implying that adsorption onto either support fails to change the electron density at the metal center or introduce an asymmetry in the electron distributions about the metal.[48] The lack of change at the metal center and the absence of a significant change in C-O vibrational energy suggest the slight changes in energy and relative intensity arise from a change in molecular symmetry on adsorption.

Although $Fe(CO)_5$ physisorbs weakly onto both PVG and the xerogel with little change in structure and electron distribution, the chemistry of the complex on each support differs. If 10^{-4} mol of $Fe(CO)_5/g$ are adsorbed onto a freshly prepared xerogel, for example, $\geq 98\%$ of the complex is oxidized within the time of adsorption.[48] At the same loading, adsorption onto xerogels dried at 85°C for 24 hours and then at 35°C under reduced pressure, $\leq 10^{-2}$ torr, for an additional 24 hours, only 6% of the iron is oxidized to Fe_2O_3.[48] The dependence on drying implies water is the oxidant. Water is ubiquitous in these porous supports, present in both physi- and chemisorbed forms.[43,47] Physisorbed water desorbs around 100°C while chemisorbed water desorbs from 100 to 500°C, and water is then evolved as the product of the silanol condensation during the shrinkage and consolidation of the matrix at temperatures ≥ 650°C.[47] One difference between PVG and the xerogels that affects the chemistry of adsorbed complexes and ultimately the optical performance of the photodeposited structure is their water content. Drying reduces the amount of water in each support, but for all practical purposes never eliminates it. Furthermore, with samples dried under similar conditions, there is generally more water present in the xerogel than in PVG.

Gradient index formation with $Fe(CO)_5$ is generally accomplished with initial loadings of $\leq 10^{-4}\,mol/g$, which corresponds to a fractional surface coverage of $\leq 10\%$ in PVG and $\leq 4\%$ in the xerogel.[13,19] At these loadings, there is no indication that adsorption of the complex changes either matrix. $Fe(CO)_5$(ads) weakly interacts with the glass surface and retains a photoreactivity equivalent to that in fluid solution. Excitation with ≤ 488-nm light leads to efficient CO loss, $\Phi_{dec} = 0.96 \pm 0.05$.[33] In vacuo, a number of intermediates of differing carbonyl content are present on PVG,[33] but in the presence of air, which are the conditions for the deposition of a gradient index, no intermediates persisting for more than a few milliseconds are detected in either matrix.[13] Exposure to CO reveals $\leq 20\%$ reversibility in PVG, but none in the xerogel. The photoproducts in PVG exhibit two Mossbauer doublets, one with an isomer shift of $0.13 \pm 0.01\,mm/s$ and a quadrupole splitting of $0.57 \pm 0.01\,mm/s$, and another with an isomer shift

of 0.52 ± 0.05 mm/s and a quadrupole splitting of 0.64 ± 0.06 mm/s (Figure 8).[32,48] The spectrum of the photoproduct in the xerogel consists of a single doublet with an isomer shift of 0.40 ± 0.01 mm/s and a quadrupole splitting of 0.95 ± 0.01 mm/s, which corresponds to octahedrally coordinated Fe^{3+} (Figure 9).[32,48] The doublet at 0.52 ± 0.05 mm/s with a quadrupole splitting of 0.64 ± 0.06 mm/s in PVG also corresponds to octahedrally coordinated Fe^{3+}, but what is surprising here is that the doublet at 0.13 ± 0.01 mm/s with a quadrupole splitting of 0.57 ± 0.01 mm/s (Figure 8) corresponds to elemental iron indicating that both elemental iron, Fe^{o}, and Fe^{3+} are formed in PVG,[34] whereas only Fe^{3+} is found in the xerogel.[32] The absence of elemental iron in the xerogel is attributed to the higher content of water in the xerogel, which results in complete oxidation of the photoproducts.

The Fe^{o}/Fe_2O_3 ratio in PVG varies somewhat from sample to sample, but $56 \pm 5\%$ of the iron photochemically deposited in PVG is present as elemental iron with the remainder present as octahedrally coordinated Fe^{3+}.[34] The ratio declines slightly during the subsequent heating and consolidation, but $45 \pm 4\%$ of the iron in consolidated PVG remains as elemental iron. Startling high numbers, considering that the photolysis and heating are carried out in air, and consolidation of PVG lead to water evolution, which is expected

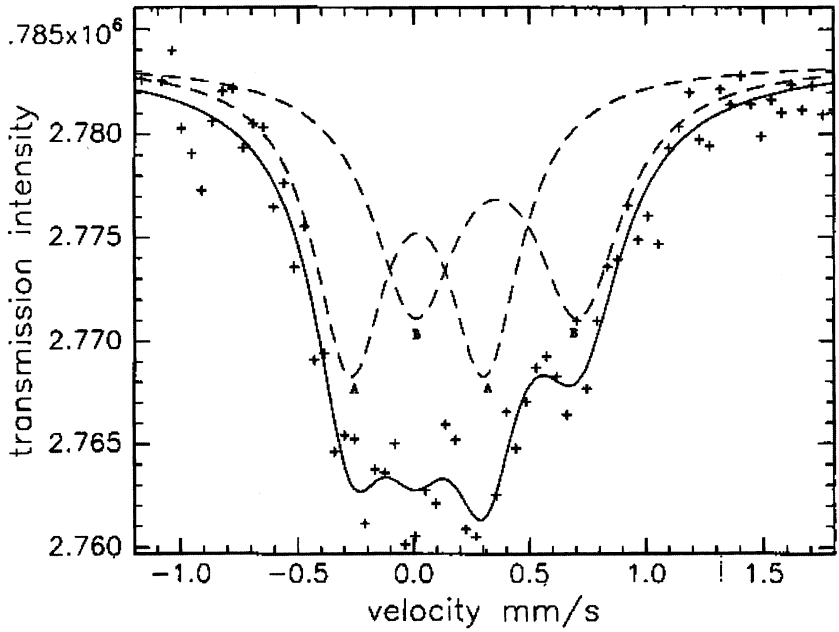

FIGURE 8 Mossbauer spectrum of iron photodeposited in PVG.

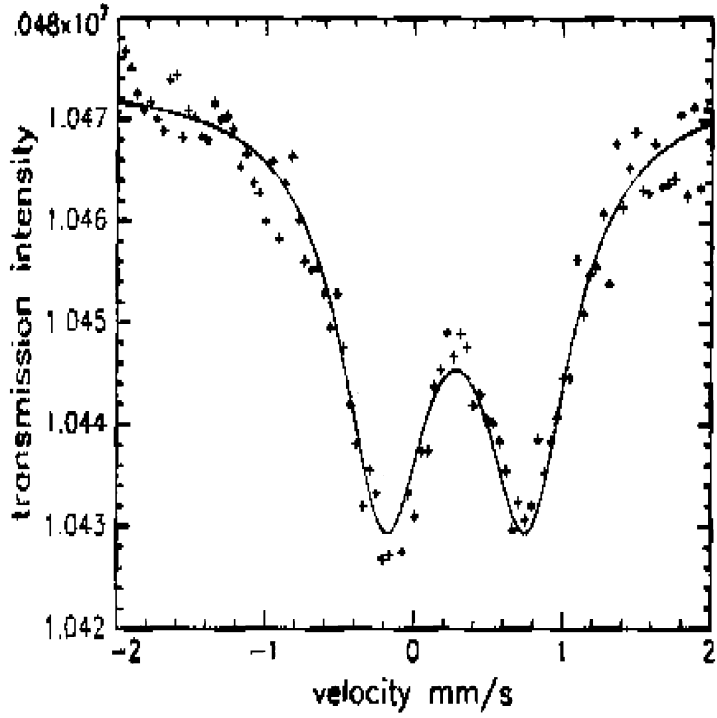

FIGURE 9 Mossbauer spectrum of iron photodeposited in TMOS/MeOH/H_2O xerogel dried at 650°C.

to oxidize atomic iron. Nonetheless, EXAFS and XANES corroborate the Mossbauer findings with the normalized intensity of the XANES pre-edge corresponding to $59 \pm 5\%$ of the iron in PVG as elemental iron after photolysis and $45 \pm 5\%$ as elemental iron in the consolidated glass.[34] The Fe^{3+} product in consolidated PVG closely resembles α-Fe_2O_3 with a central Fe^{3+} octahedrally surrounded by six oxygen atoms at a distance of 0.18 nm, while the other corresponds to elemental iron with a central iron atom surrounded by eight other iron atoms at a distance of 0.2 nm.[36]

EXAFS gives no indication of Si in either the first or second shell of atoms about a central Fe^{3+} or Fe^{o} either after photolysis or after heating and consolidation of either matrix. In fact, attempts to include Si in either the first or second shell of atoms significantly degrade the fit of the oscillatory portion of the main edge absorption.[36] Consequently, neither iron species incorporates into the silica matrix, as might be found if the metal were directly added to a melt, or is directly bonded to the PVG either covalently through Si or an O bonded to Si. Rather, both species appear to exist as distinct entities on the

surfaces of the silica nodules, suggesting that the coordinated oxygens in Fe_2O_3 derive from adsorbed water. Furthermore, since consolidation of the glass matrix occurs below the melting point of elemental iron, 1535°C, and the decomposition temperature of Fe_2O_3, 1565°C,[57] both materials are entrapped without disruption of their coordination spheres between melding silica nodules.[40]

The isomer shift, 0.40 ± 0.01 mm/s, and the quadrupole splitting, 0.95 ± 0.01 mm/s, of the photoproduct in the xerogel differ from those in PVG, but are within the range for octahedrally coordinated Fe^{3+}.[32,48] Consistent with the Mossbauer spectra, which provide no indication of Fe^o formation in the xerogel, the XANES pre-edge feature indicates all the iron in the xerogel is Fe^{3+}. Consolidating the xerogels at 1200°C broadens the Mossbauer spectrum and resolution yields two doublets (Figure 10). One is equivalent to that observed after photolysis and is assigned to octahedrally coordinated Fe^{3+}. The second, however, with an isomer shift of 0.23 ± 0.01 mm/s and a quadrupole splitting of 2.0 ± 0.01 mm/s, corresponds to tetrahedrally coordinated Fe^{3+}.[48] The relative intensities of the doublets

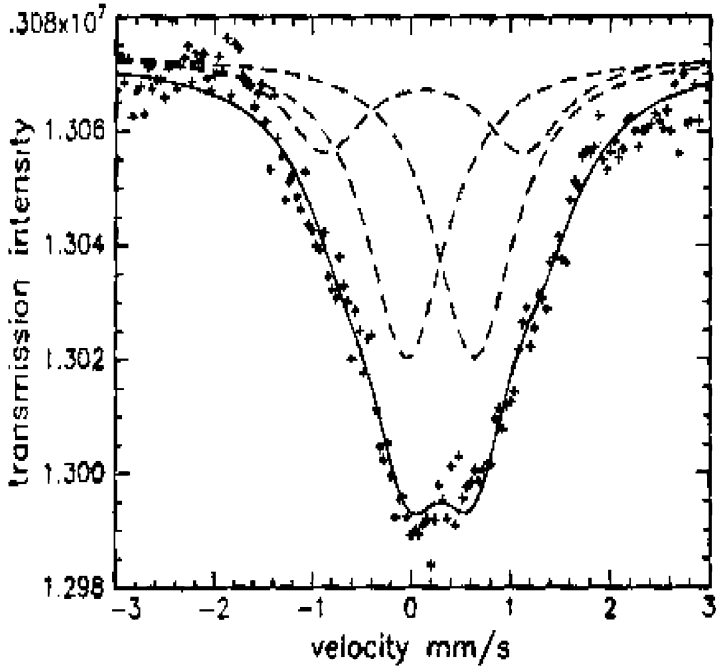

FIGURE 10 Mossbauer spectrum of photodeposited iron after consolidation of the TMOS/MeOH/H_2O xerogel at 1200°C.

indicate $77 \pm 3\%$ of the iron is present in the xerogel as octahedrally coordinated Fe^{3+} and $23 \pm 3\%$ as tetrahedrally coordinated Fe^{3+}. The XANES preedge feature, which increases to more than twice the intensity of the main absorption on consolidation, corroborates the formation of tetrahedrally coordinated Fe^{3+}, and the best fit of the oscillatory portion of the main absorption (Figure 11) occurs with 80% of the Fe^{3+} surrounded by 5.9 ± 0.1 oxygens at a distance of 0.19 nm, and 20% of the Fe^{3+} surrounded by 3.6 ± 0.1 oxygens at a distance of 0.17 nm.[48] Unlike PVG, where both Fe^{3+} and Fe^{o} are formed photochemically and the product ratio is relatively insensitive to matrix consolidation,[34] photolysis of $Fe(CO)_5$ in the xerogel produces only octahedrally coordinated Fe^{3+} and $23 \pm 3\%$ of that converts to tetrahedral Fe^{3+} on consolidation of the xerogel.

Boron oxide Lewis acid sites, designated BO_3, are present in PVG with some estimates suggesting as much as one-third of the PVG surface is boron oxide.[57,58] These are not present in the xerogel, but attributing the differences in the chemistry to their involvement has no experimental support. The Mossbauer, EXAFS, and XANES give no indication of boron bound to iron, or its presence in the second shell of atoms about a central iron atom in PVG, implying that boron is neither directly nor indirectly bound to iron[32,36] and therefore not involved in the reaction sequence. The absence of Fe^{o} in the xerogel is attributed to its higher water content, which leads to complete oxidation of the iron deposited in the xerogel. This explanation is not entirely satisfactory, however, since drying the xerogel has yet to result in Fe^{o} formation. The absence of Fe^{o} in drier samples suggests the differences in the chemistry arise from more fundamental differences in the matrices themselves. Since water is ubiquitous in both materials, perhaps the higher irregularity of the PVG surface, as compared to that of the xerogel, curtails the access of the water to the photodeposited iron and/or curtails its mobility on the PVG surface, but less so on the smoother xerogel surface, thereby allowing Fe^{o} formation in PVG but not in the xerogel.[48] The dimensions of the structural features on the PVG surface, 22 ± 1 nm, and more importantly, the dimensions of the intervening spaces, which are similar in size (Figure 2), are much larger than the cross section of water, ca. 0.15 nm.[50] Consequently, these structures are not steric hindrances in the molecular sense. Rather, the irregularity of the PVG surface may be related to the relative number of free and associated silanols present in each material.[44,45,51] The higher irregularity of the PVG surface may enhance the proximity of the silanols thereby increasing hydrogen bonding so that most exist as associated silanols. On the other hand, the smoother, less irregular xerogel surface (Figure 4) may limit silanol association and more may exist as free, individual silanols. DRIFT spectra of xerogels heated to 650°C exhibit a fairly symmetric band centered at 3725 cm^{-1}. Some asymmetry exists on the lower wave number side of the band, but the distinct shoulder in the 3650 cm^{-1} region is not present.[47] In contrast, DRIFT spectra of PVG heated to 650°C exhibit a sharp, narrow band at 3745 cm^{-1} with a distinct, broad,

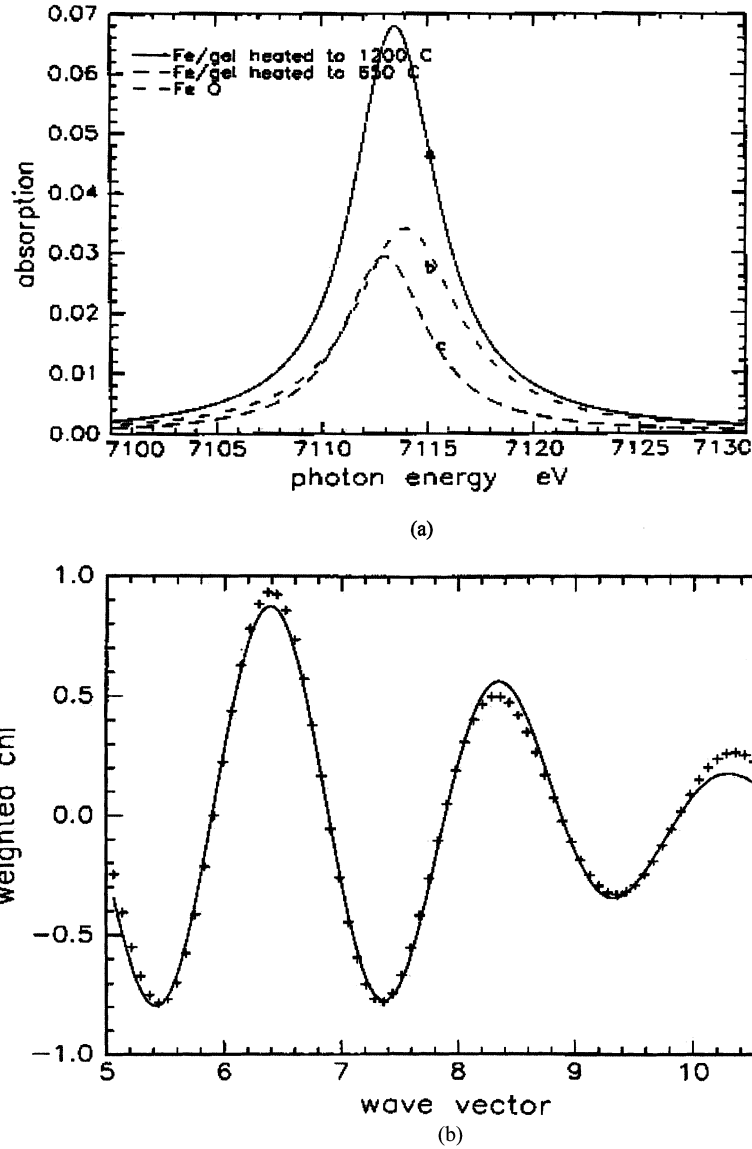

(a)

(b)

FIGURE 11 (a) XANES and (b) EXAFS spectra of photodeposited iron in consolidated TMOS/MeOH/H_2O xerogel.

asymmetry on the shorter wavelength side of the absorption.[33] The data are by no means conclusive, but they do suggest that more of the silanols present in PVG are in the form of associated silanols, whereas more of the silanols present in the xerogel are free, individual Si-OH functionalities. Offering the potential of multiple hydrogen bonds to adsorbed water, the larger number of associated silanols present in PVG may curtail or prevent the mobility of water relative to that on the smoother xerogel surface at the same temperature, where more of the silanols are present as free or individual silanols and unable to offer the same level of hydrogen bonding to the adsorbed water.

The EXAFS spectra of iron in the xerogel indicate that Si is not present in the first shell of atoms about the central Fe^{o} but are not sufficiently resolved to identify the atoms present in the second shell of atoms.[48] Assuming the oxygens coordinated to Fe^{3+} derive from water in the xerogel, as appears to be the case in PVG, the higher water content in the xerogel would be expected to favor octahedral coordination. Indeed, all the iron deposited in the xerogel via photolysis is initially octahedrally coordinated Fe^{3+}, but $23 \pm 3\%$ converts to tetrahedral coordination on heating and consolidation of the xerogel matrix.[48] Transition metals can replace silicon in silicate matrices,[59,60] and the appearance of tetrahedrally coordinated iron in these xerogels suggests that, as the temperature is raised, Fe^{3+} displaces the tetrahedrally coordinated Si in the xerogel matrix.[59] This immediately raises the question, however, as to why tetrahedral coordination occurs in the xerogel but not in PVG. It is not due to temperature since consolidation of the xerogel occurs at lower temperatures than PVG (Figure 6) and both materials are heated to 1200°C to achieve complete consolidation. Rather, it may arise from the fact that PVG, although porous, is formally a glass. Derived from a melt, PVG has been raised above its sintering temperature, and as a result achieves the stable silica structure of glass.[41] The xerogel, on the other hand, is not a glass, but a polymer derived from the low temperature condensation alkoxysilanes.[17] It has not been heated to or above its sintering temperature, and therefore has yet to achieve the stable silica structure of a glass. In fact, the difference is evident in the consolidation of the two materials. In contrast to the smooth decline in surface area as PVG consolidates, consolidation of the xerogel is preceded by a chaotic domain (Figure 6) arising from the decomposition and loss of the organic constituents of the xerogel. Consistent with the absence of tetrahedral coordination immediately after photolysis, these sites are not available during the photochemical reaction, which is run at room temperature. The samples must first be heated to 300–500°C to desorb the organic constituents from the xerogel. Even in gels dried at 500°C, the occurrence of bands at 2959 and 2852 cm^{-1}, although much lower in intensity, indicates the presence of organic substituents in the gel.[47] In fact, AFM images of xerogels dried at 500°C show sharp-edged craters in the xerogel surface (indicated by the arrow in Figure 7), suggesting that desorption of the organic components and their degradation products, which

are distributed throughout the matrix, is a violent process capable of exploding through the xerogel matrix. The violent desorption of the organic components and their decomposition products is thought to break matrix bonds, thereby opening tetrahedral sites that are filled by Fe^{3+}. Devoid of organic precursors, this chaotic domain is not present in the consolidation of PVG, which, already sintered, is composed of silica nodules that have achieved the stable silica structure of glass and are therefore less likely to form a reactive tetrahedral site.

Incorporating Fe^{3+} ions into the silica network of the xerogel, however, raises questions regarding size and charge balance. In SiO_2, silicon is formally $4+$, and Si^{4+} is 0.026 nm in diameter.[59] Fe^{3+}, 0.050 nm in diameter,[50] would occupy a larger volume, thereby creating a size imbalance in the SiO_2 matrix. Replacing Si^{4+} by Fe^{3+} also creates a charge imbalance that requires a counter ion in the matrix for electrical neutrality. The charge imbalance, in particular, is expected to change the spectroscopic properties of the incorporated ion, but, as described below, there is no unexpected spectral feature in the consolidated xerogels that might be attributed to a charge imbalance created by Fe^{3+} occupying a Si^{4+} site, and/or a counter ion in the xerogel matrix. Assuming the iron oxide formed in the xerogel exists as a distinct entity on the xerogel surface, i.e., it is a distinct iron-oxide molecule that is not bound to the silica surface, as in PVG, then it only exists on the outer surfaces of the silica nodules, as opposed to being incorporated into the nodule's silica matrix. Consistent with some form of limitation, only $23 \pm 3\%$ of the initially octahedrally coordinated Fe^{3+} converts to tetrahedral coordination on heating and consolidation of the xerogel matrix. Assuming the Fe^{3+} species exist on the xerogel surface, the structure $H_2O\text{-}Fe(O\text{-}Si)_3$ with water coordinated to the Fe^{3+} and O-Si representing oxygens of the silica framework is formally equivalent to the well-established surface silanol $HO\text{-}Si(O\text{-}Si)_3$ with a hydroxyl attached to silicon, but with the extra proton on water, as opposed to $-OH$, compensates for the Fe^{3+}-Si^{4+} charge imbalance. Furthermore, being a surface structure, it is far more capable of distortion to accommodate the larger diameter Fe^{3+} in place of Si^{4+}.[50] Experiments exploring this possibility are in progress, but one cannot help but wonder what the catalytic implications of this type of transition metal surface structure are.

Particle Growth in PVG and Xerogels

The physical properties of the iron species deposited in PVG and the xerogel are defined, to a large extent, by the thermal treatment following photolysis. For example, consolidation of the PVG samples shifts the onset of the electronic absorption to the red and converts the superparamagnetic photoproduct to ferromagnetic.[39] The xerogels show essentially identical changes in their electronic spectra, yet consolidation of the xerogel does not convert

the initially superparamagnetic photoproduct to a ferromagnet.[39] In fact, no set of experimental conditions examined to date, including initial $Fe(CO)_5$ loading, photolysis conditions, and subsequent thermal treatment, leads to a ferromagnetic impregnate in the consolidated xerogel. Recent studies of nanometer-sized particles of platinum-group transition metals and main group semiconductors clearly show that spectroscopic properties are functions of particle size.[61–66] Since the changes in the impregnate's properties in PVG and the xerogel occur without a change in sample composition, particle size and growth in these porous matrices was determined as a function of photolysis and thermal treatment of the samples and correlated with the physical properties of the deposits.

No particles ≥ 1 nm in diameter are detected by TEM in either PVG or the xerogel after photolysis, implying the photoproducts are either individual atoms or molecules or small aggregates ≤ 1 nm in diameter.[39] The latter seems the most likely, at least in PVG, since as noted above the Fe^o/Fe_2O_3 ratio declines slightly as the PVG samples are heated in air and ultimately consolidated at 1200°C, but $42 \pm 12\%$ of the iron in consolidated glass remains as elemental iron.[34] The absence of complete oxidation in PVG, specifically in the consolidated glass, where water is a consolidation product and is expected to oxidize individual Fe atoms, suggests the products are small aggregates composed of an iron core surrounded by an Fe_2O_3 cladding. Five-nm diameter iron particles generated in air, for example, react immediately to form 1–2-nm-thick oxide coatings, which prevent further oxidation of the elemental iron core.[67] Heating to 650°C increases particle diameter from ≤ 1 nm to 3–4 nm (Figure 12). Assuming densities equivalent to bulk Fe^o and α-Fe_2O_3 and equivalent numbers of Fe^o and Fe^{3+}, since the Mossbauer doublets are of the same intensity, these particles consist of a 2-nm diameter Fe^o core containing 925 Fe^o atoms surrounded by a 1-nm-thick Fe_2O_3 cladding containing 467 Fe_2O_3 molecules.[39] Consolidation at 1200°C increases the particle diameter to 10 ± 1 nm (Figure 13) with an average inter-particle spacing of 22 ± 1 nm. The diameter of the particles and their average spacing in consolidated PVG are equivalent to the initial pore diameter in porous PVG, 10 ± 1 nm, and its correlation length, 23 ± 1 nm, implying that the pore structure of PVG acts as a template for particle growth.[39] If the pore structure serves as a template, then Fe^o/Fe_2O_3 particle growth must occur below the softening and collapse of the pore structure, i.e., below 650°C, or the temperature at which PVG begins to shrink and consolidate (Figure 6). Otherwise, a range of particle sizes and spacings are expected, which is not observed (Figure 13).

Fe^o-Fe_2O_3 particle growth within the pores of the glass seems intuitive, but it raises a number of mechanistic questions as to how it occurs. Since $Fe(CO)_5$ uniformly distributes to a depth of *at least* 1500 μm in PVG (Figure 14),[13] attributing particle growth simply to the aggregation of the photoproducts requires extensive diffusion of the photoproducts. And in PVG, where photolysis leads to equal amounts of Fe^o and Fe_2O_3, diffusion

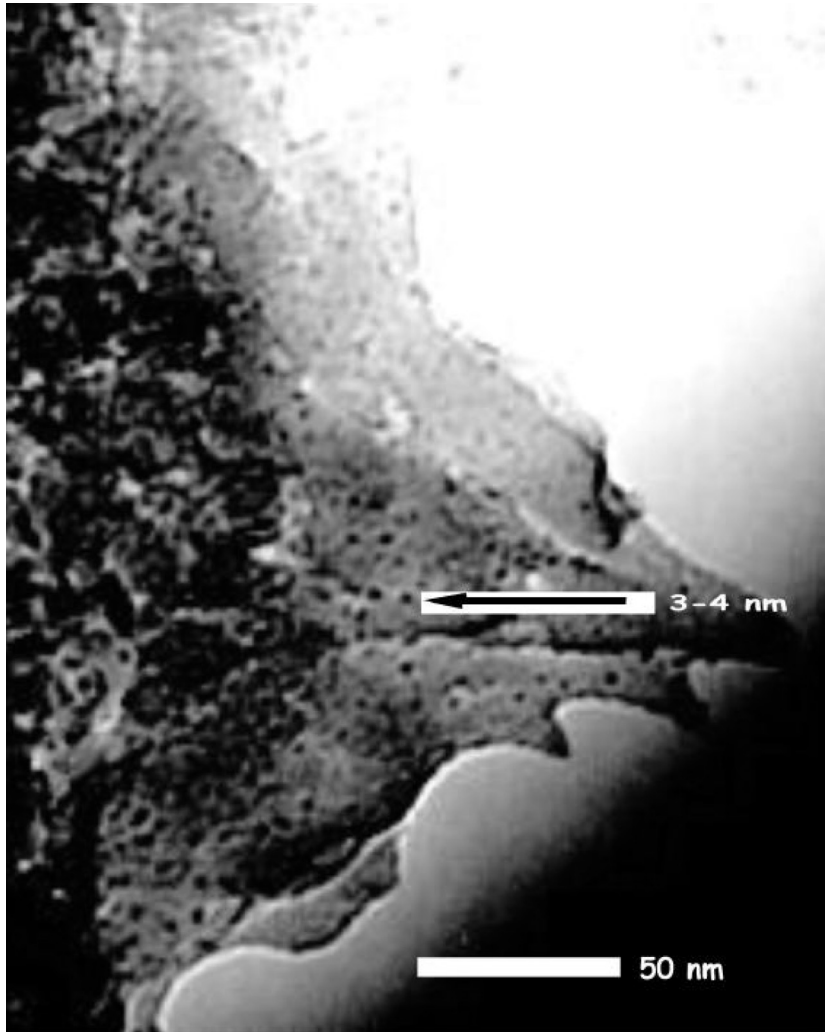

FIGURE 12 TEM of 3–4-nm diameter Fe-Fe_2O_3 particles in PVG heated to 650°C. Nodular structure of the porous glass also evident.

must occur with minimal oxidation of the elemental iron. In our opinion, small aggregates of elemental iron tumbling across the highly irregular, hydroxylated surfaces of PVG (Figure 2) without undergoing oxidation is very unlikely. Rather, PVG becomes a template for particle growth because of extensive $Fe(CO)_5$ diffusion during photolysis. As the photochemical

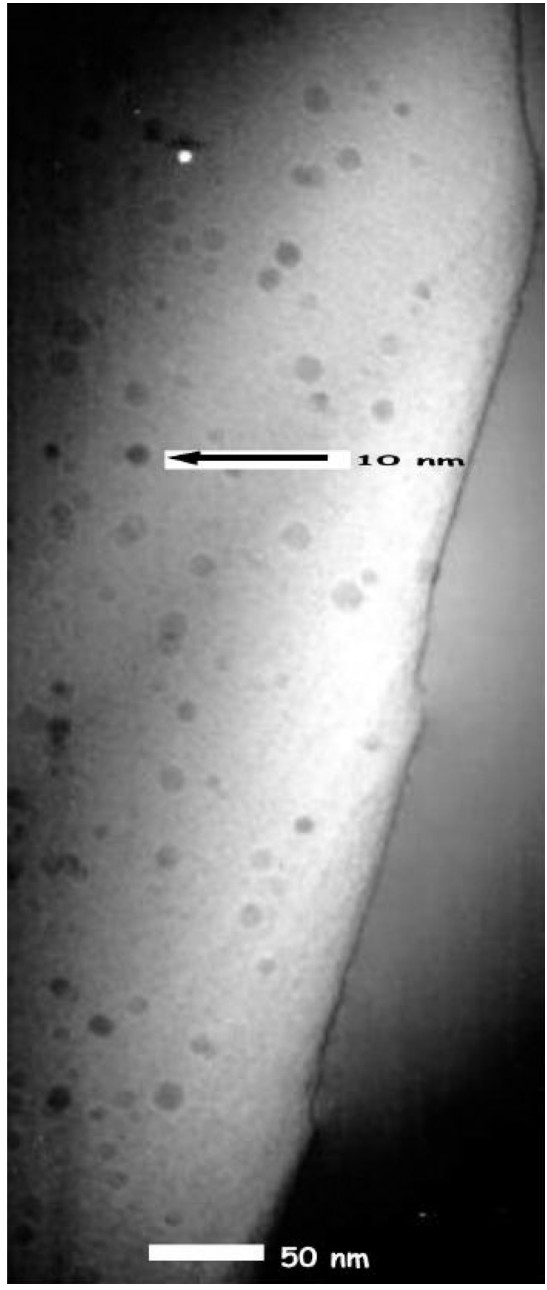

FIGURE 13 TEM of 10 ± 1-nm diameter Fe-Fe_2O_3 particles in consolidated PVG.

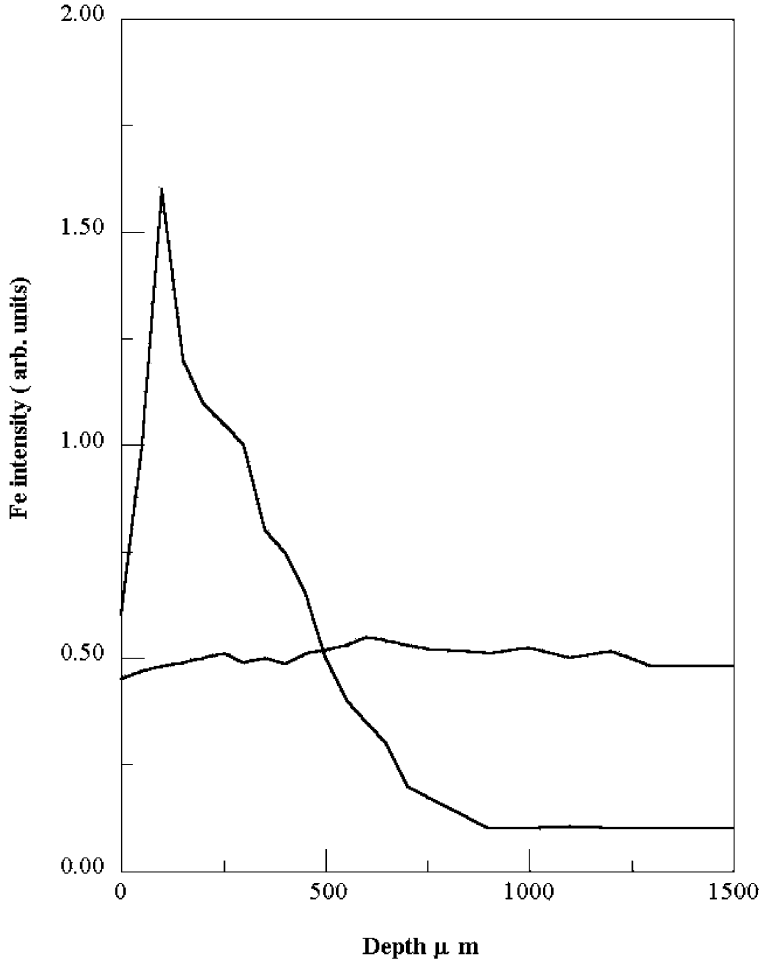

FIGURE 14 Distribution of iron in PVG before (horizontal line at an Fe intensity of 0.5) and after photolysis.

reaction consumes $Fe(CO)_5$ in the outermost volume adjacent to the exposed sample face, unreacted $Fe(CO)_5$ diffuses from the interior into the exposed region where it undergoes efficient photoinduced decomposition. $Fe(CO)_5$ diffusion is evident in milliseconds and is attributed to the volatility of the complex and its weak interaction with the surface.[33] Diffusion increases the amount of iron present in the first 100–200 μm by at least a factor of three (Figure 14), while that in the interior declines to less than 10% of that originally present.[13] A three-fold increase in iron in the

first 100–200 μm increases the loading to 3×10^{-4} mol of $Fe(CO)_5/g$ in the outer volume corresponding to fractional surface coverage of ca. 0.30, or ca. 1 $Fe(CO)_5$ molecule/nm^2. As a result, $\leq$1-nm diameter aggregates of Fe^o and Fe_2O_3 form via diffusion on the order of tens of nanometers. Furthermore, since $Fe(CO)_5$ desorbs from the glass at a relatively low temperature, further particle growth during heating and consolidation derives principally from the aggregation of the particles created photochemically. No further change in iron distribution occurs on heating or consolidation, indicating that further particle growth requires diffusion of $\leq 20\,\mu m$ (Figure 14).

$Fe(CO)_5$ diffusion during photolysis and the high quantum yield of reaction, $\Phi_{dec} = 0.96 \pm 0.05$,[33] suggest that photoinduced decomposition begins on all surfaces and therefore particle growth begins on all internal surfaces, including not only the pore surfaces but also the surfaces within the interconnecting passages. The occurrence of spherical particles, 10 ± 1-nm in diameter, with an average inter-particle spacing, 22 ± 1 nm, equivalent to the correlation length (Figure 13) suggests that, as the PVG is heated, the photoproducts becomes relatively mobile prior to the temperatures needed to collapse the pore structure of the glass.[39] Since the latter begins around 300°C (Figure 6), photoproduct mobility must initiate at a lower temperature, but higher than room temperature. Also, since the narrower, interconnecting passages collapse at a faster rate than the larger pores, and the photoproducts are not chemically bound to the surface of the melding silica nodules, collapse of the narrower passages may force the smaller particles formed within the interconnecting passages into the larger pores. Further experiments are needed to establish the controlling factors, but the results obtained in PVG point to tailoring the morphology of acid-leached porous glasses to tailor the size, and in turn the properties, of the deposit.

As in PVG, no particles are found in the xerogel after photolysis, but, unlike PVG, surprisingly no particle growth occurs during the subsequent heating and consolidation of the xerogel. TEM fails to reveal particles in xerogels heated to 650°C or in the consolidated xerogel, implying that the photoproduct, initially an octahedrally coordinated Fe^{3+} similar to the Fe_2O_3 formed in PVG, exists either as individual molecules or small aggregates ≤ 1 nm in diameter on the xerogel surface.[48] Whether $Fe(CO)_5$ diffusion during photolysis occurs to the same extent in the xerogel as it does in PVG remains to be established, but since decomposition and desorption of the organic constituents of the xerogel occurs over the 300–500°C temperature range where particle growth occurs in PVG, the absence of particle growth in the xerogel may be due the chaotic domain in the xerogel created by the decomposition and desorption of the organic components of the xerogel. Loss of the organic constituents creates a dynamic, changing surface in the xerogel that may curtail diffusion and, therefore, particle growth.[48]

Physical Properties of Fe^o and Fe_2O_3 in PVG and Xerogels

Consolidation of both matrices improves transparency in the near-IR by removing the overtones of the 3750 and 3650 cm^{-1} SiO-H bands that appear in the 1350–1400-nm region (Figure 15). Both materials exhibit $\geq 80\%$ transparency (relative to air) in the 1100–1700 nm region (Figure 15). However, transparency in the visible region declines as the samples are heated and ultimately consolidated with 50%T in both PVG and the xerogel shifting from the 300–350-nm region immediately after photolysis to the 650–700-nm region in the consolidated glasses (Figure 15). In PVG, the spectral changes occur with only slight changes in the Fe^o/Fe^{3+} ratio, implying that the loss in visible transparency is not the result of a change in chemical composition. Rather, a linear correlation between the size of the particles formed at the different temperatures and the onset of the absorption, i.e., the wavelength at which 50%T occurs (Figure 16), suggests the loss of visible transparency is due to particle growth. The Fe^o/Fe_2O_3 particle behaves as a quantum dot with its optical absorption shifting to the red as particle size increases. The results are preliminary and limited to an initial $Fe(CO)_5$ loading of 10^{-5} mol/g. Nonetheless, at this point, since the particles are considerably smaller than visible wavelengths, the decline in visible transparency in PVG is not attributed to light scattering but to the quantum dot effect, where the optical absorption shifts to the red as particle size increases.

Essentially identical spectral changes occur during heating and consolidation of the xerogel (Figure 15), but TEM analyses of the samples fail to reveal any particles in samples heated to 650°C or consolidated at 1200°C, indicating that the particle diameter in the xerogel remains ≤ 1 nm regardless of whether the sample is heated or consolidated. These results clearly challenge the assignment of the spectral changes in PVG as due solely to a quantum dot effect. On the other hand, particle size does correlate with magnetic properties. Photodeposition in both PVG and the xerogel yields a superparamagnetic impregnate that converts to a ferromagnetic material on consolidation of PVG, but not on consolidation of the xerogel.[68] Heating PVG to 1200°C yields a spherical particle 10 ± 1 nm in diameter (Figure 12) consisting of an elemental iron core surrounded by the oxide. Assuming equal numbers of Fe^{3+} and Fe^o, since the relative intensities of the Mossbauer doublet are the same, and densities equivalent to the bulk materials, the diameter of the elemental iron core is calculated to be 6.8 nm with a 1.6-nm-thick Fe_2O_3 coating. The core diameter is slightly smaller than the reported minimum diameter, 8.0 nm, necessary to achieve sufficient coercivity at 300 K to maintain magnetic alignment in Fe^o particles deposited in SiO_2.[69] However, it is in excellent agreement with the diameter calculated from the linear relationship between the diameter of the iron core, d_c, and total particle diameter, d_t, i.e., $d_c = (0.85\, d_{total} - 1.5)$ nm.[70] The median particle diameter found in PVG, 10 ± 1 nm, yields a diameter of the iron core of 7.0 ± 0.8 nm, suggesting that

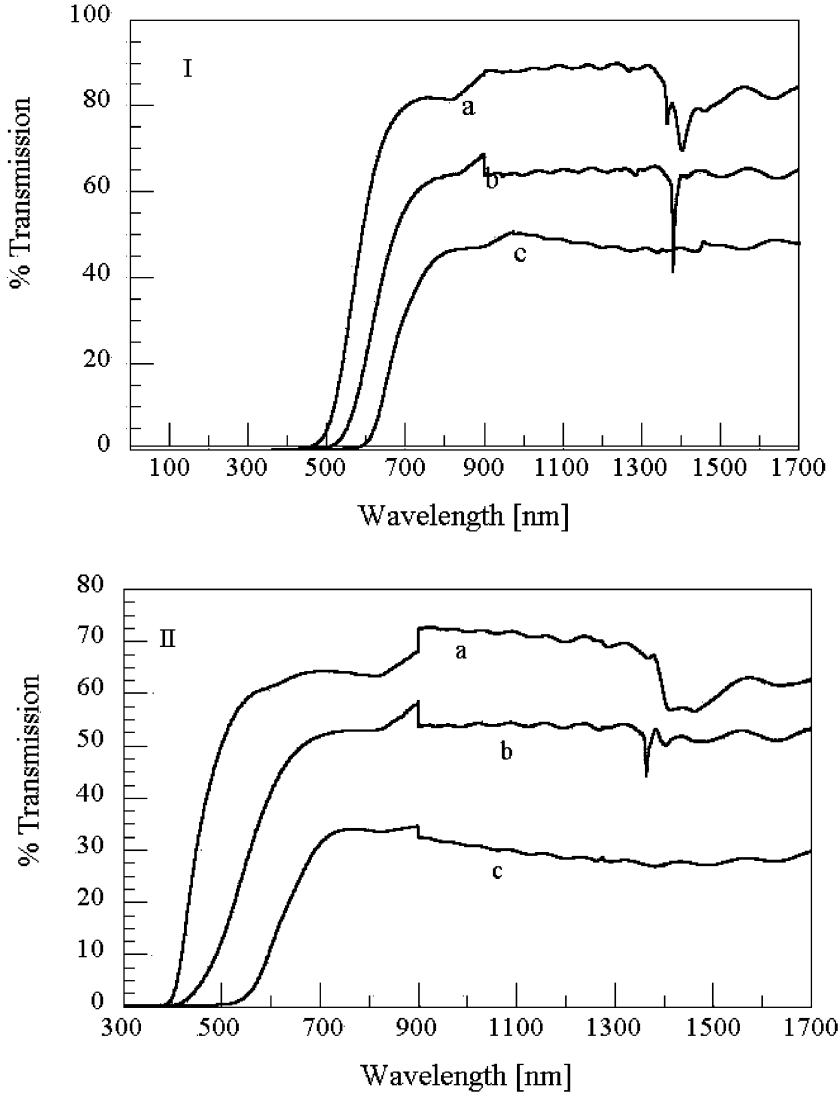

FIGURE 15 Absorption spectra of iron in (I) PVG and in (II) TMOS/MeOH/H_2O xerogel as a function of subsequent heating. The letters a, b, and c refer to spectra recorded after photolysis (a), after heating to 650°C (b), and after consolidation at 1200°C (c).

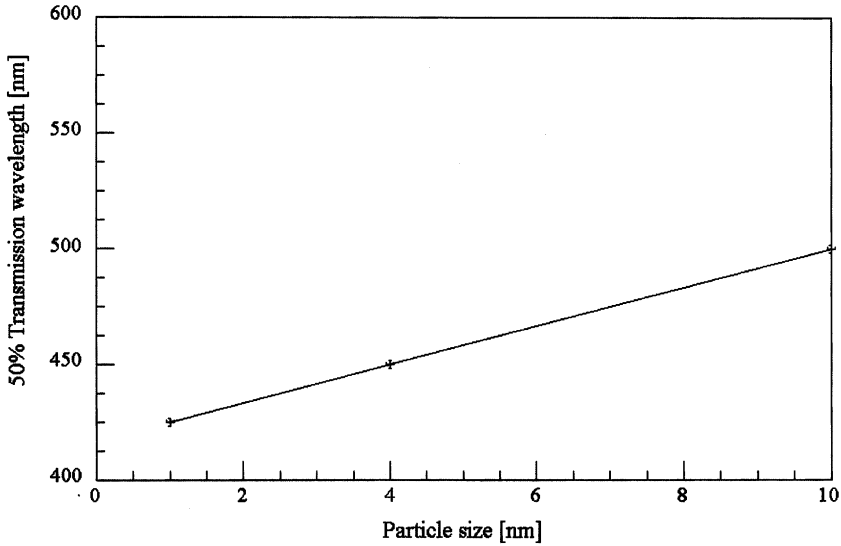

FIGURE 16 Wavelength at which 50%T occurs vs. Fe-Fe_2O_3 particle diameter in PVG.

the appearance of ferromagnetism in this Fe^o-Fe_2O_3 -PVG system arises from the increase in particle size that occurs during consolidation of PVG. The lack of particle growth in the xerogel accounts for the absence of the conversion from superparamagnetic to ferromagnetic on consolidation of the xerogel.

PVG acts as a template for Fe^o-Fe_2O_3 particle growth, but the conversion to a ferromagnet is not simply a process of filling the pores with 3–4-nm particles (Figure 12) to create a 10 ± 1-nm diameter particle (Figure 13). Simple aggregation of smaller particles retains the magnetic properties of the smaller particles, i.e., superparamagnetism. Furthermore, particle growth occurs at temperatures below softening and loss of the pore structure of PVG, yet no samples examined to date have changed from superparamagnetic to ferromagnetic at temperatures below the softening of the glass, i.e., $\leq 650°C$. Instead, conversion from superparamagnetic to ferromagnetic requires heating to 1200°C, i.e., the temperature required to consolidate the glass. Consequently, conversion to a ferromagnet requires an additional thermal step. The surface irregularity that would be expected from the simple aggregation of smaller particles is not evident in 10 ± 1 nm diameter particles in the consolidated glass (Figure 13) that exhibit ferromagnetism.[39] At the resolution of the TEM experiments, ≤ 0.5 nm, the particles appear to be spherical, suggesting that the higher temperatures required to consolidate the glass also meld the individual, smaller, 3–4 nm diameter Fe^o-Fe_2O_3

particles (Figure 12) into a single particle. This melding of the Fe^o-Fe_2O_3 particles appears to be a sintering since it occurs more than 300°C below either the melting point of elemental iron, 1535°C, and the decomposition temperature of Fe_2O_3, 1565°C. Formation of the larger 10 ± 1-nm diameter particles requires the aggregation of 23–24 of the 3–4-nm diameter particles. Since formation of the larger particles occurs with little change in the Fe^o/Fe_2O_3 ratio, aggregation and melding of the smaller particles must occur without compromising the integrity of the oxide coatings about the elemental iron cores.[39] The initial thought was that the larger particle was simply a larger version of the smaller particles, i.e., a 7.0 ± 0.8 diameter Fe^o core surrounded by 1–2-nm-thick Fe_2O_3 cladding. However, this structural form requires the iron cores of the smaller particles to diffuse together into a single interior unit, while the oxide coatings of the smaller individual particles diffuse to the exterior of the larger particle. Since the melting points of Fe^o and Fe_2O_3, 1535 and 1565°C, respectively, exceed the 1200°C these samples are heated to, a symmetric structure composed of a spherical Fe^o core surrounded by a uniformly thick Fe_2O_3 layer is discounted. Rather, agglomeration and melding must create a number of smaller Fe^o units dispersed within an Fe_2O_3 matrix (Figure 17). Assuming the ferromagnetism arises from the Fe^o units, since

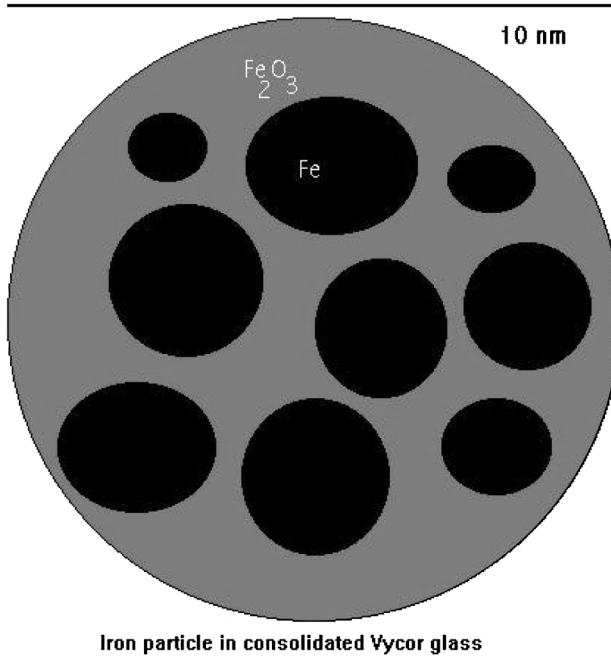

FIGURE 17 Dispersion of Fe^o aggregates within Fe_2O_3 matrix in consolidated PVG.

α-Fe_2O_3 is anti-ferromagnetic,[39] its occurrence in this type of structure implies magnetic coupling through the Fe_2O_3 matrix since the individual Fe^o units must be less than the 8.0-nm diameter needed for sufficient coercivity to maintain magnetic alignment at 300 K.[69] Dispersing the 1–2 nm diameter Fe^o aggregates throughout the Fe_2O_3 matrix increases the surface area of the oxide relative to that of elemental metal and reduces the separation between the two. Both enhance the exchange anisotropy between the oxide and the dispersed aggregates of the elemental metal[69,71–73] which would contribute to the high coercivity, 965 kG, found for these 10 ± 1-nm diameter particles formed in consolidated PVG.[39]

Photodeposition of Tin Oxides in Porous Vycor Glass and Porous Xerogels

Tin oxides possess larger band gaps than iron oxides and therefore offer higher transparency at shorter wavelengths. SnO_2 has a band gap of 4.3 eV, for example, and tin is also a glass modifier.[74,75] However, most tin compounds that could serve as photoactive precursors absorb in the UV at wavelengths shorter than both PVG and the xerogels where 50%T is generally around 350 nm.[33] Consequently, competitive absorption by the glass matrix limits the depth of photodeposition and therefore the depth of the gradient index that can be created within either matrix. Nevertheless, the potential of higher transparency at shorter wavelengths led to the examination of the photodeposition of tin in these porous matrices, principally in PVG. Of the commercially available, photochemically active tin compounds, $(CH_3)_3SnI$ possesses the lowest energy absorption, exhibits the highest efficiency photoreaction, and is reasonably volatile, thereby allowing for desorption of the unreacted compound. Previous studies of the photochemistry of $(CH_3)_3SnI$ establish the primary photochemical step as homolytic cleavage of the Sn-I bond followed by radical coupling and quantitative formation of I_2 and $[(CH_3)_3Sn]_2$.[76] Although both products desorb from the glass prior to consolidation and therefore should not lead to a refractive index gradient in consolidated PVG, 254-nm photolysis of $(CH_3)_3SnI$ adsorbed onto PVG yields changes in refractive index similar to those obtained with $Fe(CO)_5$. Consequently, the adsorption of $(CH_3)_3SnI$ and its thermal and photochemical behavior on PVG were examined to identify the reaction pathway leading to gradient index formation.[35,77]

Tin compounds are coordination labile with coordination number and structure functions of the medium in which they are being examined.[78–80] Unlike $Fe(CO)_5$, which physisorbs onto PVG and the xerogel without change, adsorption of $(CH_3)_3SnI$ onto PVG reduces the intensity of 3744 cm^{-1} SiO-H bands and leads to the appearance of a broad band centered at 3555 cm^{-1} and methyl bands at 2993 and 2917 cm^{-1}. The electronic spectrum of the complex, which exhibits an LMCT absorption at 234 nm

($\varepsilon = 3.45 \times 10^3\,M^{-1}\,cm^{-1}$) in hexane, shifts to 230 nm when adsorbed onto PVG. In spite of the small shift, Mossbauer spectra of adsorbed $(CH_3)_3SnI$ yield a ratio of the quadrupole splitting, 3.14 mm/s, relative to the isomer shift, 1.06 mm/s, of 2.96 that falls within the range expected for five or six coordinate tin compounds.[35] Further insights into the molecular changes accompanying adsorption come from the behavior of the complex in the presence of ethanol and hexanol, which, like PVG, possess hydroxyl moieties. In ethanol and hexanol, the low energy LMCT absorption of $(CH_3)_3SnI$ occurs at 218 nm and 221 nm, respectively, and the absorption at 234 nm in hexane shifts to shorter wavelength as either alcohol is added to a hexane solution of the complex. Job's plots constructed from hexanol titrations of hexane solutions of the complex reveal the formation of a 1:1 $(CH_3)_3SnI$-C_6H_5OH adduct. Formation of the adduct is not accompanied by loss of a methyl group, an iodine atom, or loss of the alcohol O-H stretch, thereby precluding a displacement reaction and formation of an alkoxide. Instead, the alcohol coordinates to the tin without loss of the hydroxyl proton, and formation of the alcohol adduct shifts the $(CH_3)_3SnI$ LMCT band to shorter wavelength and the alcohol O-H vibration to lower energy. Formation of the ethanol adduct, for example, shifts the ethanol O-H vibration from 3635 to $3350\,cm^{-1}$.[35] Along with the Mossbauer data, which indicate the formation of a five- or six-coordinate tin compound, the similarity of the spectral changes found on addition of the alcohols with those occurring on adsorption onto PVG point to the formation of a surface-bound adduct. Retention of the SiO-H band indicates Sn does not replace the silanol hydrogen, but interacts with the lone pairs on the silanol oxygen. Originally, the surface adduct was thought to be five coordinate since the average silanol number of PVG, taken to be 5 $SiOHs/nm^2$, requires an unusually long Sn-O bond for six coordinates.[35] As a result, the broadness of $3550\,cm^{-1}$ band was attributed to a range of interactions reflecting the local topology and/or the number of free or associated silanols at the adsorption site. However, the recent AFM results taken together with the DRIFT spectra of PVG suggest, as previously noted, that the majority of the silanols present in PVG are associated.[48] Being associated, the silanols are more closely spaced and could allow for the formation of both five- and six-coordinate surface adducts, in which case, the broadness of the SiO-H band may reflect the presence of both five- and six-coordinate adducts on the glass surfaces. Whether due to local topology and/or coordination number, the key point is that the complex binds to the glass surface and this changes the bonding in $(CH_3)_3SnI$, and, in turn, its reactivity.

A 254-nm photolysis of $(CH_3)_3SnI$ in hexane leads to homolytic cleavage of the Sn-I bond and quantitative formation of I_2 and $[(CH_3)_3Sn]_2$ with the quantum efficiency of bond cleavage declining with increasing wavelength.[76] The quantum yields of $(CH_3)_3SnI$ disappearance in hexane decreases from 0.32 ± 0.05 at 254 nm to 0.11 ± 0.06 at 310 nm and $\leq 10^{-3}$ at 350 nm. Competitive absorption by the glass precludes equivalent measurements for the adsorbed complex, but relative yields as a function of excitation wavelength

clearly show that the quantum yield of reaction of the adsorbed complex declines with increasing wavelength.[35] The products of reaction on the glass surface, however, differ from those in hexane solution. A 254-nm photolysis of the adsorbed complex leads to the immediate appearance of I_2 and I_3^-, whereas photolysis in hexane yields only I_2.[35,76] Mossbauer spectra of the photolyzed sample resolve into two absorptions: a singlet with an isomer shift of 1.16 mm/s, which establishes $[(CH_3)_3Sn]_2$ formation, and a doublet with an isomer shift of 1.12 mm/s and a quadrupole splitting of 3.05 mm/s. The latter is assigned to $(CH_3)_3$Sn-OSi, where -OSi represents coordination to the glass matrix, since the isomer shift, 1.12 mm/s, and quadrupole splitting, 3.05 mm/s, fall with the range reported for trialkyltin alkoxides.[35,81] Despite the structural changes that occur on adsorption, the wavelength dependence of the reaction, decreasing efficiency with increasing wavelength, and the lack of a dependence on O_2 suggest that the photoreactivity of the adsorbed complex initiates from the same excited state as that in hexane solution, i.e., the $(CH_3)_3$SnI LMCT state corresponding to a $5p(I) \rightarrow \sigma^*_{Sn\text{-}I}$ absorption at 234 nm in hexane and 230 nm on the glass.[82] Nevertheless, the reaction products are indicative of homolytic cleavage of the Sn-I bond rather than the redox products expected from an LMCT state.

The isomer shift of $(CH_3)_3$SnI in hexane, 1.28 mm/s, shows that the Sn is partially positive and therefore the Sn-I bond is polarized in the ground state, $Sn^{\delta+}$-$I^{\delta-}$. The smaller isomer shift and larger quadrupole splitting for the adsorbed complex indicates that adsorption further polarizes the Sn-I bond making the tin more positive and the I more negative.[35] The largest polarization of the Sn-I bond occurs on formation of the ethanol adduct, $(CH_3)_3$SnI-OHC_2H_5. In fact, the polarization is so great the adduct reacts spontaneously with I_2 at room temperature to form a [$(CH_3)_3$Sn-$OHC_2H_5^+$, I_3^-] ion pair.[35] Since the ground state is polarized in each medium, an LMCT transition creates a more uniform charge distribution in the excited state, and the more uniform charge distribution is thought to favor homolytic cleavage of the $(CH_3)_3$Sn-I bond. This pictorial representation is consistent with recent calculations on $(CH_3)_3$SnI, which show that the state populated by the $5p(I) \rightarrow \sigma^*_{Sn\text{-}I}$ absorption is dissociative with respect to the Sn-I coordinate, leading directly to radical products.[82] In hexane, the radicals quantitatively couple to form $[(CH_3)_3Sn]_2$ and I_2.[76] The formation of both products on the glass surface indicates the same reaction pathway for the adsorbed complex. However, the immediate appearance of I_3^- suggests a fraction of the radical pairs undergo a secondary thermal electron transfer leading to $(CH_3)_3$Sn-O-Si and HI on the more polar glass surface,[83] and the HI reacts with the I_2 formed photochemically to form I_3^-.[35] The fraction of the initially formed radical pairs that undergo subsequent electron transfer is small, but from the point of view of patterning a refractive index gradient it is this small fraction that does not desorb from the glass during consolidation that changes the refractive index of the glass.

Unlike gradient indices created with $Fe(CO)_5$, where 50%T shifts to the red as the samples are consolidated, the transparency of the refractive index gradients created by photolysis of $(CH_3)_3SnI$ hardly changes during consolidation of the glass. After photolysis, 50%T occurs in 350-nm region and remains in that region throughout the consolidation of the glass.[40] Transparency in the 1400–1500-nm region is also $\geq 80\%$ relative to air and unaffected by consolidation.[40] In spite of the lack of change in the absorption spectra, Mossbauer reveals changes in the composition of the tin impregnate. Heating to 650°C yields two absorptions (Figure 18). One exhibits an isomer

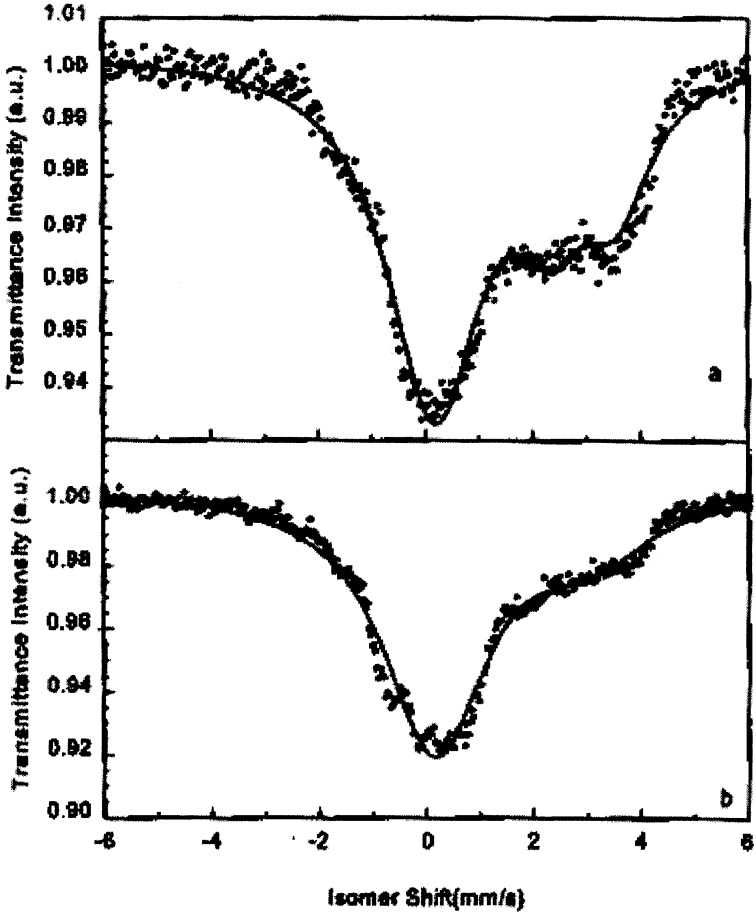

FIGURE 18 Mossbauer spectrum of photodeposited tin after heating to (a) 650°C and (b) 1100°C. Solid line represents computer fit of the data.

shift of ≤ 0.03 mm/s, and quadrupole splitting, 0.01 mm/s, relative to the SnO_2 source, indicating formation of an Sn(IV) oxide very similar to SnO_2.[40] The other exhibits an isomer shift, 2.80 mm/s, and quadrupole splitting, 1.28 mm/s, indicative of an Sn(II) oxide, SnO.[40,74,75] An intense band at 486.2 ± 0.2 eV in the x-ray photoelectron spectra corroborates SnO_2 formation, while a lower energy band at 485.4 ± 0.2 eV confirms concurrent SnO formation.[40,84] Eventually all of the $(CH_3)_3$Sn-O-Si photoproduct converts to SnO_2, but at shorter times, the Sn(IV)/Sn(II) ratio, calculated from the relative intensities of the two XPS absorptions, varies, increasing from 2.8 ± 0.3 after heating to 650°C to 12 ± 1.0 after heating in air to 900°C and then declining to 3.8 ± 0.4 after heating the sample to 1100°C in air.[40] The latter value agrees with a value of 3.5 ± 0.4 calculated from the relative intensities of the Mossbauer absorptions. SIMS confirms that these ratios are biased by Sn diffusion (Figure 19) with the amount of tin in the first 5 nm of the sample (relative to Si) increasing by 4.5 ± 0.4 upon heating from 650°C to 900°C. Since the Sn(IV)/Sn(II) ratio increases by the same amount, 4.3 ± 0.4, the increase in the ratio at 900° is attributed to the diffusion of tin from the interior of the glass to the outer volumes of glass, where it reacts with air to form principally SnO_2. Regardless of the Sn(IV)/Sn(II) ratio, diffusion increases the amount of tin in the outer 5 nm of the glass. However, the total amount of Sn in the outer 5 nm of the glass declines on heating to 1100°C (Figure 19) suggesting that as much as 80% of the tin could be evaporating from the samples during sintering. The mechanism by which this occurs is not known, but it is worthwhile to note that the temperature required to consolidate PVG, 1200°C, exceeds the decomposition temperatures of SnO, 700–950°C,and SnO_2, 1127°C. If tin is being lost on consolidation, then the amount of tin needed to produce a gradient index in the consolidated glass is significantly smaller than currently thought since current data are based on the initial $(CH_3)_3$SnI loading.

Photodeposition of tin produces changes in refractive index similar to those obtained with $Fe(CO)_5$, but in a number of cases, particularly with higher loadings, $10^{-5} - 10^{-4}$ mol of $(CH_3)_3$SnI/g of PVG, the glass becomes opalescent, and small-angle x-ray scattering from samples heated to 1200°C yields a scattering peak corresponding to a correlation length, 22.7 nm, equivalent to the correlation length of the porous glass, 23 ± 1 nm.[40,46] Unlike the results with $Fe(CO)_5$, where PVG consolidates about particles as large as the pore diameter, 10 ± 1 nm, the correlation length indicates the glass containing tin is not consolidating even though it is heated above the sintering temperature of the glass, 1105 ± 18°C.[47] Although Sn diffuses into the outer volumes of the glass during heating, the lack of consolidation is not due to the formation of larger SnO or SnO_2 particles, about which the glass can not consolidate. TEM analyses of the samples prepared with initial $(CH_3)_3$SnI loading of $10^{-5} - 10^{-4}$ mol/g, which correspond to fractional surface coverages of 0.12 to 1.2%, fail to reveal any particles in the samples after photolysis or in samples heated to 1200°C, indicating that the SnO

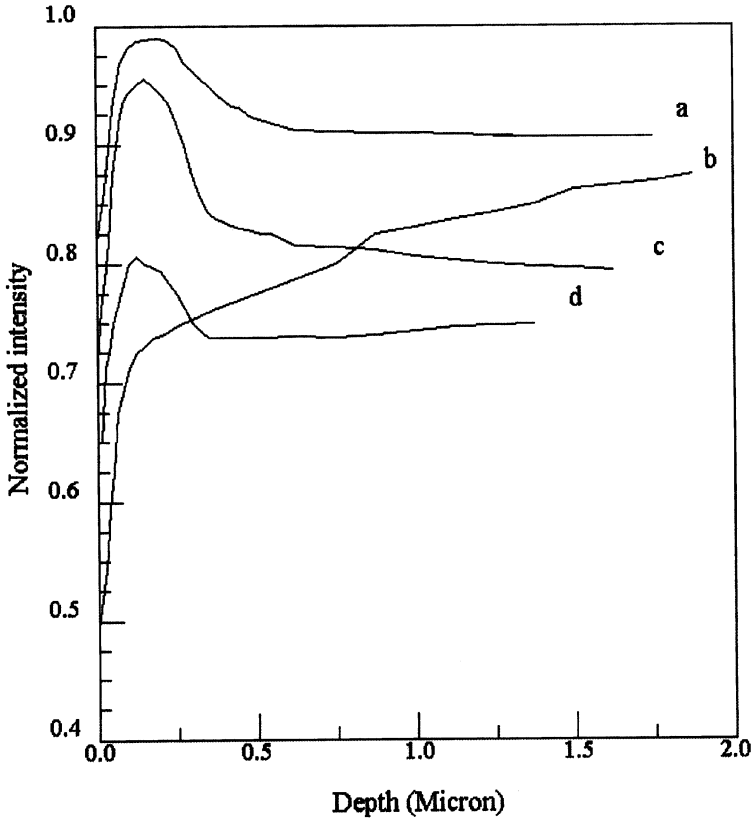

FIGURE 19 Cross sectional distribution of boron in PVG samples heated to (a) 650°C and (c) 1100°C, and in samples impregnated with $(CH_3)_3SnI$ heated to (d) 650°C and (b) 1100°C.

and SnO_2 are $\leq$1-nm in diameter. Unlike $Fe(CO)_5$, where the glass acts as the template, heating leads to particle growth, and the glass consolidates about Fe^o/Fe_2O_3 particles as large as the initial pore diameter, 10 ± 1 nm, heating the photolyzed $(CH_3)_3SnI$ impregnate samples fails to induce particle growth or result in consolidation of the glass. More surprising, microscopic examination of patterns created microlithographically with $(CH_3)_3SnI$ and then heated to 1200°C reveals structures in the exposed regions extending 2–4 μm above the glass surface. Tests with luminescent probes indicate these structures and the underlying regions retain a high absorptivity in comparison to the unexposed regions, implying the surface structure and the underlying

glass remain porous, whereas the surrounding regions consolidated to a non-porous glass.

Effect of Tin Oxides on the Consolidation of Porous Vycor Glass

Densification of PVG initiates at 650°C with a sharp decline in surface area occurring from 700 to 1050°C (Figure 6) as the surface structures (Figure 2) and the silica nodules (Figure 1) meld together. Considering the glass transition temperature, 848 ± 20°C, and the sintering temperature, 1105 ± 18°C, heating to 1200°C should produce consolidation but fails to do so in the presence of the photodeposited tin. Instead, heating creates a porous structure extending 2–4 μm above the glass surface.[40] These structures can be scrapped from the glass, and X-ray diffraction of the collected material yields an intense peak at $2\theta = 28.3$°C establishing that this material is highly oriented, crystalline H_3BO_3.[40] Although acid leaching removes most of the borate from PVG, some estimates suggest that as much as one-third of the surface of the leached glass remains covered by borate.[57] H_3BO_3 formation only in the photolyzed regions of the glass suggests that the photodeposited tin promotes the loss of boron from the glass matrix. The displaced boron diffuses to the outer surfaces of the glass where it reacts with moisture to form H_3BO_3 on the glass surface.

The changes in tin and boron distribution during heating (Figure 19) support a tin-promoted loss of boron. The amount of tin relative to silicon in the first 5 nm of PVG increases by 4.5 upon heating from 650°C to 900°C (Figure 19). Over the same temperature range, boron diffuses from the interior to the exterior volumes of PVG where it increases the amount of boron by as much as a factor of two in the first 200–500 nm of the glass (Figure 19). In glasses containing 1.7×10^{-5} mol of $(CH_3)_3SnI/g$ and annealed under identical conditions, heating to 650°C increases the amount of boron in the outer volumes of the glass, but the total amount of boron in the samples containing tin is 30–40% less than that in samples without tin. Furthermore, heating to 1100°C significantly reduces the amount of boron in the outer volumes of glasses containing the photodeposited tin relative to those volumes that do not contain photodeposited tin, confirming that the photodeposition of tin promotes boron loss (Figure 19). Whether the tin-promoted loss of boron is stoichiometric or occurs by some other process is not known, but a tin-promoted loss of boron will produce a tin distribution that is the inverse of the boron distribution, i.e., regions high in tin will be low in boron. Traces of Zr, which come from the refractory tank liner during the manufacture of PVG, prevent quantitating the tin distribution, but x-ray fluorescence measurements of the cross-sectional distribution of tin in PVG (Figure 20) show the largest amount of tin adjacent to the outermost surfaces of the glass, where SIMS measurements (Figure 19) indicate the largest depletion of

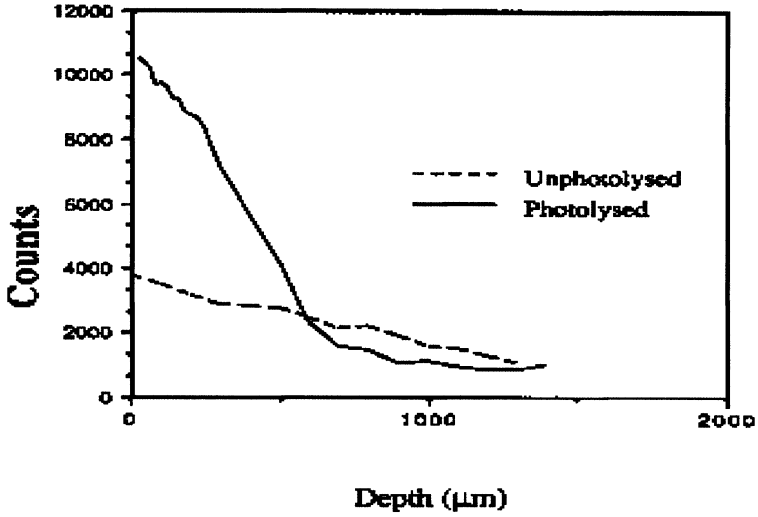

FIGURE 20 X-ray fluorescence of tin in the photolyzed and unphotolyzed regions of a PVG sample heated to 1200°C as a function of depth into the sample.

boron. The details of the mechanism are not clear, but oxidation of the photoproduct, $(CH_3)_3Sn\text{-}OSi$ and the subsequent changes in the Sn(II)/Sn(IV) ratio occur over the same temperature range as the change in boron distribution within the glass, suggesting that oxidation of the tin and the boron loss are coupled processes. Indeed, studies of a tin-doped SiO_2-Al_2O_3-B_2O_3 system show that increasing the B_2O_3 content at the expense of the SiO_2 content reduces the amount of Sn(IV) relative to the amount of Sn(II). In this case, boron is thought to occupy tetrahedral sites coordinated to four matrix oxygens, thereby decreasing the number of sites available to Sn(IV).[74] In PVG, the opposite occurs with the photodeposited Sn(IV) apparently displacing the boron from tetrahedral coordination sites in the glass. Since the boron phase separates during cooling of the PVG melt and the boron remaining in the acid-leached glass is on the surfaces of the silica nodules, tin displacement of boron appears to yield a tin species on the surface of the SiO_2 nodule and bound to at least one silica oxygen. At elevated temperatures, $\geq 650°C$, the displaced boron diffuses from the outer volumes of the glass to the outer surface where it reacts with moisture in the atmosphere to form crystalline H_3BO_3. In microlithography experiments, H_3BO_3 does not appear as individual particles on the glass surface, but as a micron-sized structure equivalent in size to the region exposed to the UV light and extending 2–4 μm above the surface of the glass.

X-ray fluorescence shows that tin is also present in the unexposed regions. This tin arises from a fraction of the adsorbed precursor $(CH_3)_3ISn$-OHSI that thermally decomposes on the glass surface either during heating and/or desorption from the glass. Since SnO and SnO_2 are the only tin species detected in the heated and consolidated glass, thermal decomposition of $(CH_3)_3ISn$-OHSI must also lead to SnO and SnO_2. However, the amount of tin present in the unexposed regions of the glass, i.e., the amount from the thermal decomposition of $(CH_3)_3SnI$, is less than half that in the exposed regions. Assuming that loss of boron is in some manner proportional to the amount of tin present, then the larger amount of tin in the photolyzed region reduces the boron content in the exposed regions more than that in the unexposed regions. The viscosity and, in turn, rate of consolidation of the glass are proportional to the amount of boron in the glass,[41,43,54] which, in turn, is proportional to the amount of tin present. Regardless of the amount of tin present, eventually all samples of PVG consolidate when heated at 1200°C for a sufficiently long enough period of time. However, at shorter times, the differences in tin content created photochemically, called the pattern contrast, changes the rates of consolidation sufficiently to open a time window (Figure 21) that can be exploited to create regions of porosity within an otherwise consolidated glass. Within the range of loadings examined in these experiments, 4.2×10^{-7} to 9×10^{-5} mol of $(CH_3)_3SnI/g$ of PVG, the largest difference in the rate of consolidation occurs with an initial loading of 1.7×10^{-5} mol of $(CH_3)_3SnI/g$ of PVG. With this initial loading, SEM analysis of the cross-section of the porous regions created photochemically show that the porosity extends 6–8 μm into the glass.[47] Further experiments are needed to quantitate the amount of tin needed to optimize the differences in the rates of glass consolidation since, as noted above, as much as 80% of the tin could be evaporating from the samples during annealing, but the results of these experiments clearly show that the photodeposition of tin, in addition to creating a refractive index gradient, can be exploited to pattern regions of porosity in a consolidated glass. Obviously, these regions differ in composition from the remainder of the glass, but this difference does not appear to be sufficient to produce significant changes in spectral and photophysical properties. The absorption and emission spectra of Rhodamine 6G adsorbed into these regions, for example, are identical to those of the dye adsorbed into the untreated glass and very similar to the absorption and emission spectra of the dye in methanol solution (Figure 22), indicating a microenvironment within these regions very similar to that in untreated glass, or a hydroxylated solvent.[40] The ability to pattern regions of porosity within an otherwise consolidated glass overcomes one of the major drawbacks of using glass as a medium for integrated optics. Glass is a refractory, and retaining porosity within an otherwise consolidated glass opens the door to incorporating reagents network that are unable to withstand the consolidation temperatures of glass into an optical.

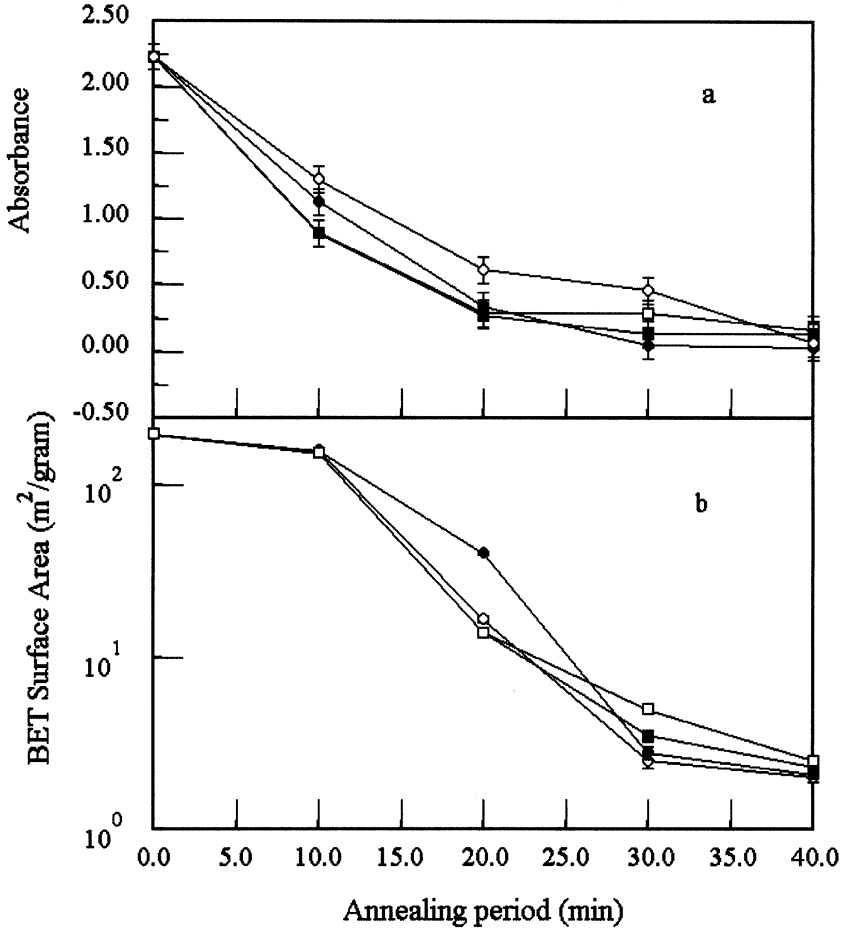

FIGURE 21 (a) Absorbance of Rhodamine 6G adsorbed into PVG, and (b) BET surface area of the PVG samples as functions of time the sample is heated at 1100°C. Unimpregnated PVG (○); PVG impregnated with 4.2×10^{-6} mol of $(CH_3)_3SnI/g$ (●); PVG impregnated with 1.7×10^{-5} mol of $(CH_3)_3SnI/g$ (□); PVG impregnated with 9.0×10^{-5} mol of $(CH_3)_3SnI/g$ (■).

Optical Structures

Waveguides

A waveguide is equivalent to an optical fiber except that it exists within a substrate that usually serves two purposes: it is the cladding for the waveguide

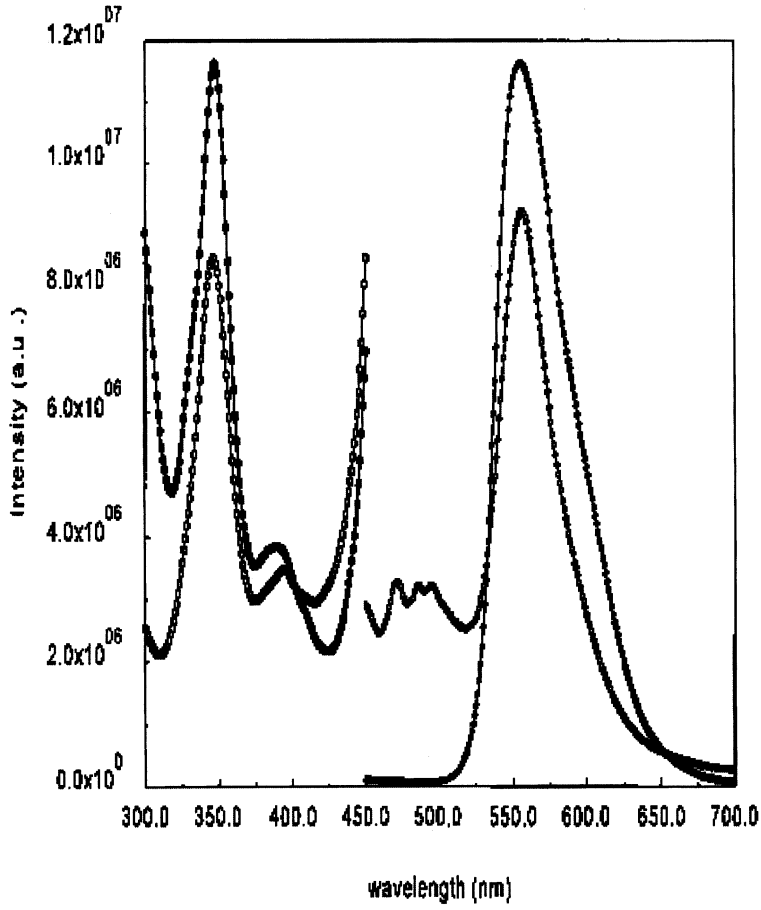

FIGURE 22 Excitation (■) and emission (•) spectra of Rhodamine 6G in methanol solution, and excitation (□) and emission (○) spectra of Rhodamine 6G adsorbed into porous regions created by the photodeposition of tin in PVG.

core and the support in which, or on which, other components of an optical network are assembled.[24,85–92] Photodeposition of a metal and/or metal oxide creates a region of higher refractive index that functions as the core and guides the light within the substrate. In general, the refractive index of the regions containing the photodeposited metal and/or metal oxide increases with initial $(CH_3)_3SnI$ or $Fe(CO)_5$ loading. However, more recent studies of the dependence of the refractive index on initial $Fe(CO)_5$ loading (Figure 23)

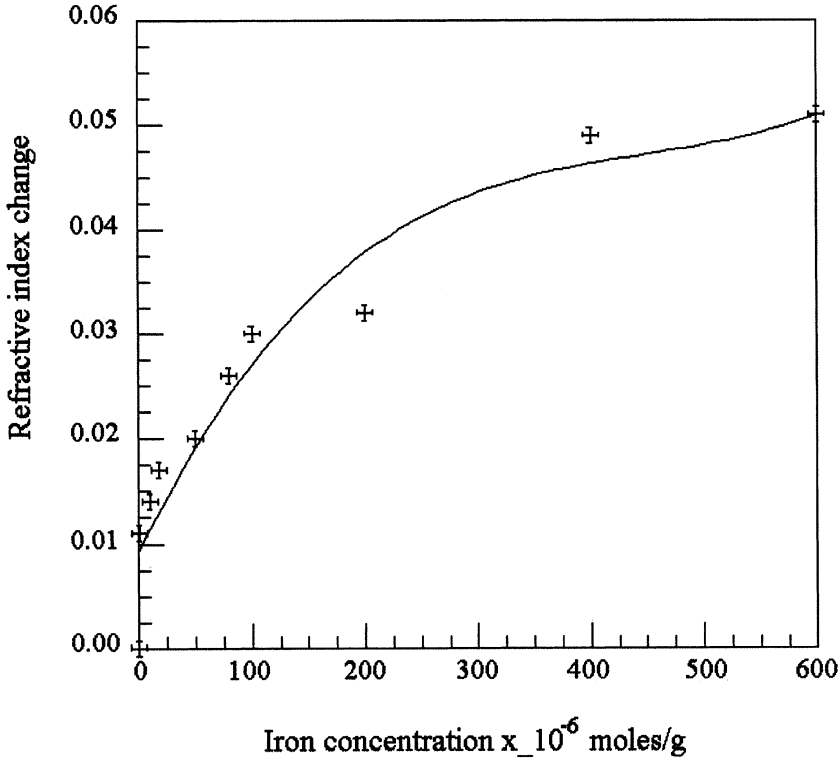

FIGURE 23 Change in the refractive index of PVG, Δn, as a function of initial $Fe(CO)_5$ loading.

show that an initial steep dependence on initial loading declines at higher $Fe(CO)_5$ loadings. Current experiments are fitting the Lorenz-Lorentz equation, Eq. 2, to this observed dependence in an attempt to determine the relative contribution of density and polarizability to the observed change in refractive index.[25,26] Identifying the principal contributor to the change in refractive index allows the largest Δn per unit metal and/or metal oxide deposited and most likely the highest optical performance since the latter can decline with higher precursor loadings.

To minimize losses due to absorption by the impregnate and scattering from the irregular surfaces of the consolidated xerogels, the optical performance measurements described here were obtained for structures created by photolysis of $(CH_3)_3SnI$ adsorbed onto polished PVG. The structures are composed of SnO_2 photopatterned in PVG and consolidated at 1200°C. Although exhibiting 50%T in the 350–400 nm region, the transmissivity of

these waveguides at 632 nm declines with increasing path length (Figure 24), yielding a loss coefficient of 0.6 dB/cm.[24] Since SnO_2 is transparent at 632 nm, the decline in transmissivity is attributed to light scattering, but not scattering from individual SnO_2 particles, since the individual SnO_2 particles are ≤ 1 nm in diameter in the consolidated glass and much smaller than the measuring wavelength, 632-nm. Rather, losses are thought to arise from other sources. First, the data in Figure 24 were obtained prior to understanding the effect of tin on PVG consolidation (see above). Particularly with the longer waveguides, some of the losses may arise from scattering due to incomplete consolidation of the PVG matrix. Other sources of loss may be lateral losses and/or scattering losses at the cladding-core interfaces. Optical microscopy reveals irregular interfaces, with the irregularity considerably less than the width of the core. Nevertheless, this irregularity will contribute to scattering losses and lower transmissivity. Further experiments are needed to establish the causes of these losses, but even with an improvement in transmissivity, when compared to loss coefficients of currently available optical fibers, which can be as low as 2×10^{-5} dB/cm, the data clearly emphasize the point that these photodeposition techniques are best suited to the creation of high density systems composed of small elements in close proximity, i.e., integrated optics. In fact, the error in transmissivity (Figure 24) shows that reproducibility of these photodeposition techniques declines with increasing size.

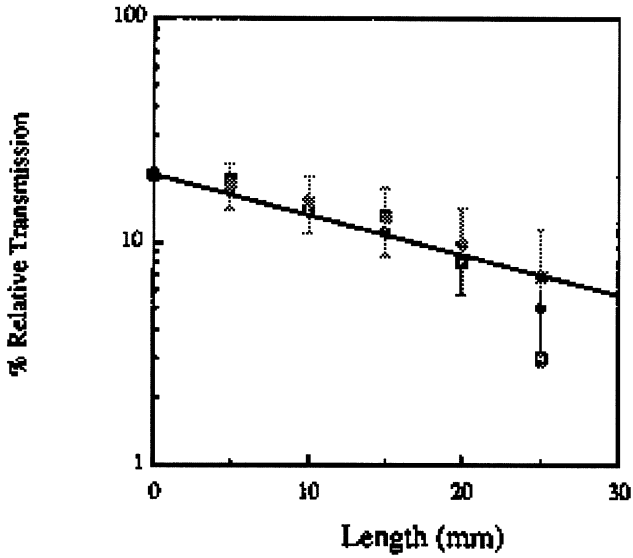

FIGURE 24 Transmission of 632-nm light through an SnO_2 waveguide photopatterned in PVG and consolidated at 1200°C as a function of waveguide length.

Waveguide bends

Waveguide bends are an integral component of all but the simplest optical circuits, and, as a result, a crucial component of circuit design.[93] Usually, the minimum allowable radius of curvature is dictated by radiation losses rather than the limits of the fabrication technique, and this appears to be the case with these photodeposition techniques. Although any angle can be created, power losses quickly increase with increasing angle. The relative power transmitted through photodeposited tin oxide waveguides connected through a 2.54 cm radius of curvature illustrates the loss as the angle between the input and output portions of the guide increases (Figure 25). Power losses in these bends are thought to reflect the irregularity of the interface between the photodeposited core and the surrounding glass cladding as described above for the straight waveguides. The more irregular the interface, the more likely the guided light encounters an interface, particularly in a bend, at less than critical angle and is lost. Since the metal oxide is initially deposited in the pores of the glass and the glass is then consolidated, the irregularity of the interface may arise from the random pore structure and is, therefore, a consequence of the morphology of the substrate in which the deposition occurs.

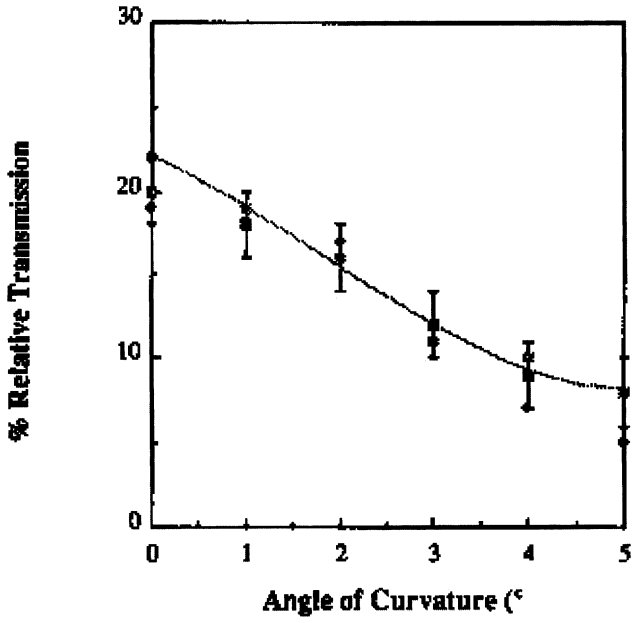

FIGURE 25 Transmission of 632-nm light through a curved SnO_2 waveguide photopatterned in PVG and consolidated at 1200°C as a function of the angle of curvature.

Consequently, improvements in power transmission in this type of structure may require tailoring the morphology of the porous glass as opposed to changing the photoactive precursor, or the photodeposition techniques.

Optical Couplers

"Y" and "star" couplers distribute power from an incoming waveguide into two or more branches (Figure 26). Like bends, these "optical couplers" are key components of more complex optical circuits.[94,95] A photodeposited Y coupler consisting of a 40-mμ-wide input waveguide branching into two 20-mμ-wide output waveguides distributes light among both legs. The ratio of power transmitted through the right branch, P_R, relative to that transmitted through both branches, $P_R + P_L$, declines as the angle between the branches increases (Figure 5). Care was taken to maximize the power transmitted through both branches, but in these short path length structures, the output power distribution is very dependent on the details of launching the light into the input waveguide. Small changes in the introduction of the light into the input leg produce large changes in the power distribution among the output legs.

The problem is more apparent in star couplers where input power is distributed among more output guides.[94,95] For example, power distribution amongst the seven output guides of 1:7 star coupler composed of a 40-micron-wide input waveguide and seven 10-micron output waveguides is visually apparent. Because of the design, three branches of increasing angle on either side of a central guide, the majority of power continues through the central output waveguide. As with a Y coupler, the power

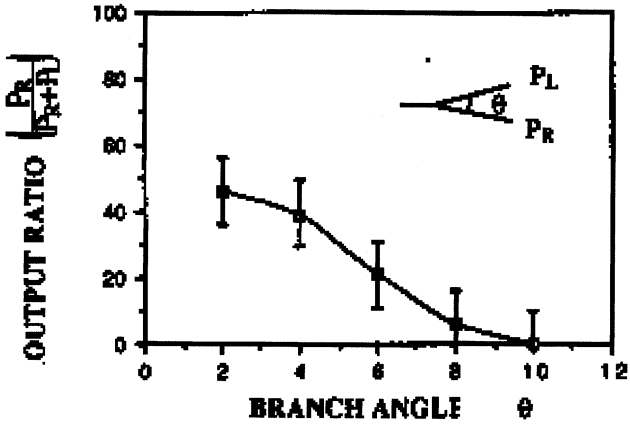

FIGURE 26 Relative ratio of 632-nm light transmitted distributed among a "Y" branch as a function of branching angle.

distributed among the branches declines as the angle between the branching waveguides and the input waveguide increases. As a result, the power distributed to outermost branches is even more susceptible to how the light is launched into the input guide. Depositing a scattering center at the junction of the waveguides, and improving the transmissivity of the individual waveguides, will improve the distribution of light among the output guides. In spite of the current limitations, these prototype structures clearly illustrate the advantages of these photodeposition techniques with respect to design flexibility at smaller dimensions, better device reproducibility, and higher power transmission than can be realized by fusing, tapering, lapping, or gluing optical fibers.

An extension of the Y optical coupler is the Mach-Zehnder interferometer, which consists of two Y couplers aligned horizontally with the branching legs connected with straight waveguides. Mach-Zehnder interferometers as small as 100 μm from branch point to branch point have been photodeposited in PVG. As found with the Y couplers, the distribution of the incoming light between the two legs of the interferometer is very dependent on how the light is launched into the input waveguide, making it difficult to achieve a uniform distribution of the light among the two branches. Nevertheless, it is obvious that the majority of the optical losses are due to scatter of the incoming light at the initial branch point.

Microlense Arrays

Photodeposition is ideally suited to the creation of microlense arrays, which are expected to have applications in digital optics.[96] The optical properties of the array can be varied by the Δn produced and design parameters such as lens shape and spacing. Figure 27 illustrates an array of 50 μm^2 square microlenses created photolithographically by the photodeposition of tin oxide in PVG. While photodeposition offers a number of advantages, it also presents challenges that must be incorporated into the element design and their creation by these photochemical techniques. Specifically, the initial deposition affects subsequent deposition and therefore the optical performance of the deposited structure. This is readily apparent in a 30 × magnified side view (Figure 28) of an array of 100-μm diameter microlenses photodeposited on the end of a 2.5-mm diameter PVG rod. The rod is cut along the rod axis perpendicular to the face onto which the lenses are photodeposited. The darker regions pointing into the body of the rod are the regions of higher refractive index created by the photodeposition of tin. The excitation light was parallel to the long axis of the rod and the intention was to create parallel regions of higher refractive index down the core of the rod. Instead, the initially created change in refractive index focuses the subsequent light, thereby limiting the subsequent excitation to regions defined by the initially deposited 100-μm diameter lens and its initial focal length, which in this particular sample is 0.66 ± 0.14 mm. The long line down the center of the rod is

FIGURE 27 Optical micrograph of an array of $50 \times 50\,\mu m$ photodeposited SnO_2 microlenses in consolidated PVG.

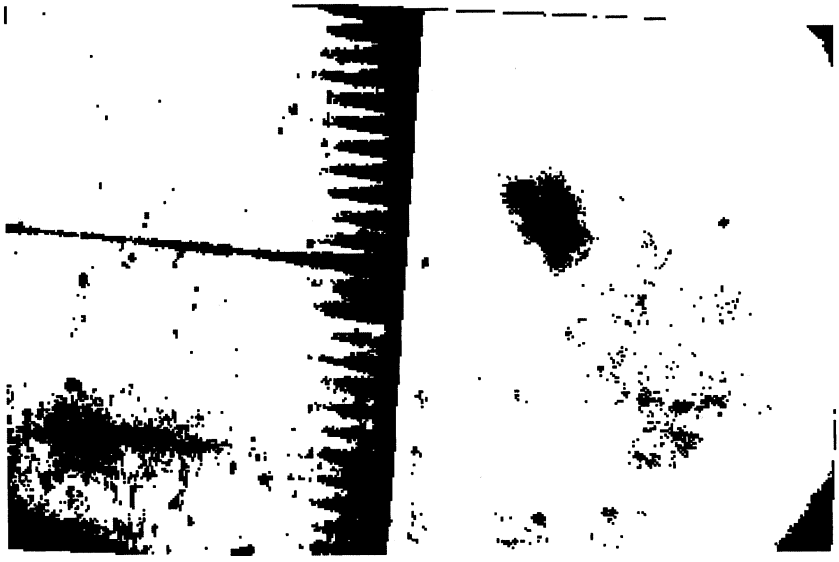

FIGURE 28 Optical micrograph of the side view of $30 \times 30\,\mu m$ SnO_2 lenses photodeposited on the end of a PVG rod and consolidated at 1200°C. Rod cut along its length perpendicular to the face on which the lenses are photodeposited.

not due to photochemical deposition, but a difference in glass density arising from the acid-leaching process. Larger lens structures, such as a Fresnel lens consisting of a concentric circles of higher refractive index, are less susceptible to the nonlinearities of the photodeposition. As expected, the finer the dimensions of the structure deposited, the more the deposition becomes susceptible to nonlinearities arising from either changes in the refractive index induced during the course of the photodeposition, or, as described below, precursor diffusion during photodeposition. The latter is particularly evident in the photodeposition of a Bragg grating.

Bragg Gratings

Bragg gratings consist of micron-spaced, parallel regions of differing refractive index and/or transparency that function as line apertures diffracting white light into its component colors. The deposition of these structures was carried out to establish "proof of concept," but also to use the structure itself to determine the resolution that can be achieved with these photodeposition techniques, the factors that affect pattern resolution, and the affect of consolidation on pattern resolution.[97–99]

Although gratings of equivalent resolution, i.e., the number of lines/mm, are accessible in both PVG and the xerogels, this discussion focuses on gratings deposited in PVG via 488-nm photolysis of $Fe(CO)_5$ since the polished surfaces of these glasses minimize differences due to surface scattering. Nevertheless, PVG is a porous material and an immediate concern was scattering by pore-glass interfaces throughout the PVG samples. Measurements of the cross-sectional intensity distribution of a laser beam before and after passing through PVG, however, show that scattering due to the pore structure of PVG does not limit resolution, at least on a length scale of $\geq 10\,\mu m$.[96] On this length scale, resolution is also independent of the method of deposition. Gratings deposited by either laser writing, photolithography, or holography consist of a series of well-defined exposed regions, which appear as dark lines in the optical micrographs (Figure 29), separated by well-defined unexposed regions. Each diffracts white light into its component colors and exhibit a number of diffraction orders when an He-Ne laser is passed through the grating. Nevertheless, optical performance depends on the method of deposition.

Lithography and holography yield uniform gratings where optical performance is independent of the position on the grating where diffraction is measured.[99] Gratings deposited by laser writing, which involves moving the sample back and forth across a focused laser beam in micron-sized steps, however, are less uniform with optical performance dependent on the position on the grating where diffraction is measured. In fact, the difference is visually apparent as a difference in the contrast between the exposed and unexposed regions with the contrast much larger in the initially deposited regions and smaller in the regions deposited later on. This difference in pattern contrast translates into significant differences in optical performance. For example, more than two higher-order maxima are visible on either side of the He-Ne fundamental when the laser beam is passed through the initially deposited region, but higher-order maxima are not visible when the beam is passed through regions deposited later on. The change in optical performance is attributed to $Fe(CO)_5$ diffusion occurring during the laser writing process.[97] Time-resolved experiments establish that, as $Fe(CO)_5$ in the outermost volumes of PVG is photochemically consumed, unreacted complex rapidly diffuses into the depleted regions.[33] Diffusion is rapid, and during photolysis results in changes in iron distribution spanning hundreds of microns.[13] Since the quantum yield of $Fe(CO)_5$ decomposition is essentially unity, $\Phi_{dec} = 0.96 \pm 0.05$,[33] and the excitation intensity used in the laser writing procedure, ca. $10^4\,W/cm^2$, is high, the concentration gradient created by photolysis draws unreacted $Fe(CO)_5$ into the exposed region, thereby reducing the amount of complex in the next region to be exposed a few microns away. Individually, the decrease in the amount of $Fe(CO)_5$ in the next volume to be exposed is small, but in depositing the thousands of lines needed to create a 2.5-cm $\times$ 2.5-cm grating, the cumulative effect is substantial and most pronounced in the last regions of the gratings to be deposited where the contrast between the exposed and unexposed regions is smallest.

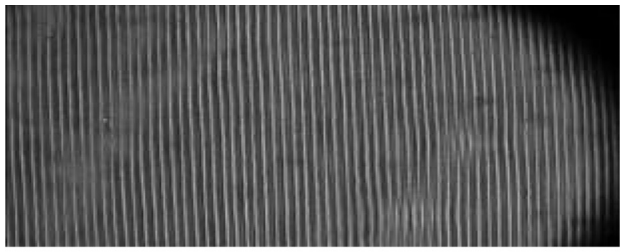

(a)

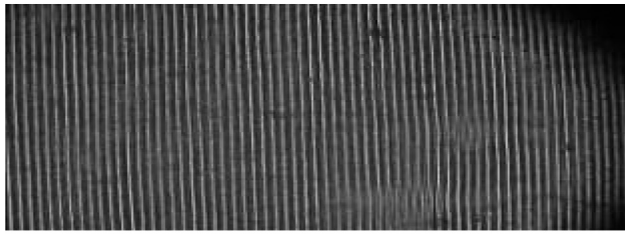

(b)

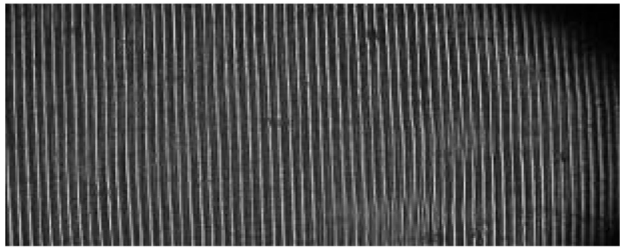

(c)

FIGURE 29 Bragg gratings photodeposited by (a) laser writing, (b) holographically and (c) photolithographically.

Since diffraction depends on the difference in optical density and refractive index between the exposed and unexposed regions, the reduction in pattern contrast due to precursor diffusion reduces the number of diffraction orders observed and their relative intensity. Reducing the excitation intensity by a factor of two does not reduce the differences in optical performance in the

different regions, implying that this is an inherent limitation of a repetitive deposition procedure using a volatile, weakly adsorbed precursor. Exposing the entire sample simultaneously, photolithographic and holographic deposition are not subject to this constraint.[99] In fact, diffusion of the unreacted precursor during photolysis occurs at all locations, thereby improving optical performance by improving pattern contrast uniformly across the entire sample. Because of the differences in pattern contrast, however, comparisons between gratings created photolithographically or holographically and those created by laser writing are limited to measurements in the first regions created by laser writing.

Pattern resolution is independent of the deposition technique.[99] Whether created by laser writing, holography, or photolithography, line patterns with line spacings of 50, 20, and 10 μm appear as sharp, well-defined exposed and unexposed regions (Figure 29). Each diffracts white light into its component's colors with dispersion of the resolved colors increasing as the line spacing decreases. Consolidation reduces sample volume by 30–35%, but it occurs without loss of pattern resolution. The decline in line spacing on consolidation, 13%, agrees with that calculated assuming isotropic consolidation, 12.8%, which supports the current picture of PVG as a porous material with a random pore structure uniformly dispersed throughout the glass.[99] Consequently, the decline in a specific dimension can be calculated from the initial dimensions of the sample and the total reduction in sample volume. In other words, the change in the dimension relevant to optical performance, i.e., the line spacing, or the decline in sample dimension perpendicular to the photodeposited lines that occurs on consolidation becomes a design parameter to improve optical performance. Although consolidation does not affect pattern resolution, line spacing or the number of lines that can be photodeposited/mm cannot be increased indefinitely. In both photolithographic and holographic deposition, pattern resolution declines rapidly with line spacings of ≤ 5 μm. Differences in refractive index or optical density are visible through an optical microscope and the photodeposited images continue to diffract light, but the exposed and unexposed regions are less well defined with the distinction between the two regions becoming blurred.[99] Unlike photolithography, where line spacing and line width are defined by the mask, in the laser writing procedure, line spacing is controlled by the computer-stepping motor, whereas line width is defined by the excitation wavelength, 488 nm, or ca. 0.5 μm. Some deviation is to be expected due to the uncertainty of focusing the excitation onto the irregular surface of PVG (Figure 1). Nevertheless, in all laser writing experiments, attempts to reduce line width and/or line spacing below 5 μm led to a loss of image resolution equivalent to that found in the photolithographic and holographic deposition experiments. Loss of pattern resolution at the same dimension, regardless of method of deposition, suggests that scattering of the excitation by the irregularities of the glass surface, and/or the pore structure limits the resolution that can be achieved by these deposition procedures. Since the

dimensions of the irregularities on the surface of the SiO_2 nodules (Figure 2), ca. 26 nm, are smaller than the excitation wavelength, 488 nm, the principal source of the scattering is thought to be the SiO_2 nodules defining the pore structure. As illustrated in Figure 30, these nodules scatter the incoming excitation not only at the outermost glass-air interface, but also at the other air-SiO_2 interfaces defined by the internal pore structure. Resolution within these porous glass matrices, therefore, is thought to be a function of, and limited by, the morphology of the glass matrix in which the deposition occurs. Experiments testing these ideas and exploring alternative approaches to overcome this limitation are in progress, but scattering by and within the matrix differentiates photopatterning in porous glass from that in a homogeneous medium such as a polymer. Except for the scattering at the polymer-air interface, the polymer is a homogeneous material with an optical uniformity on the length scale of the excitation light wavelength. Scattering does not occur within the bulk, and the chromaphores are uniformly distributed throughout the polymer. Other factors limit the resolution in a polymer, but, in general, the homogeneity of the polymer matrix allows images of smaller dimensions than those accessible in porous glass. Consequently, Bragg gratings photodeposited in a polymer more closely approach the line spacings found in

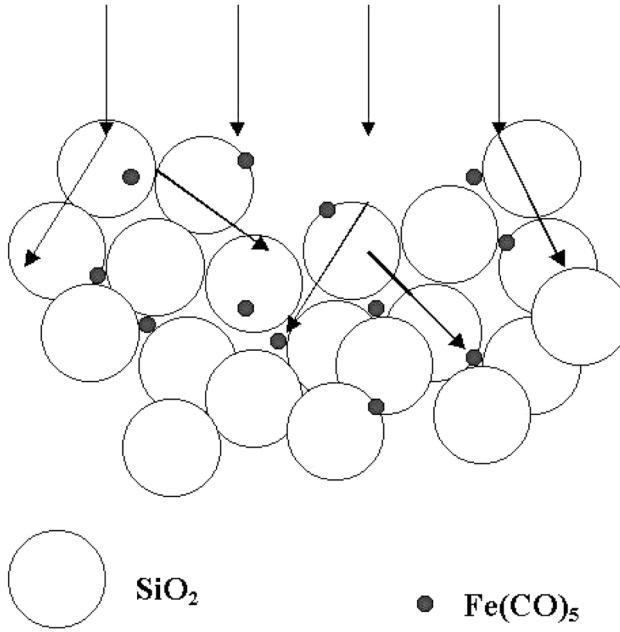

FIGURE 30 Scattering of the photolyzing light by the SiO_2 nodules making up PVG and the base-catalyzed xerogels.

conventional grooved gratings. For example, a Bausch & Lomb grooved grating blazed at 500 nm has 1300 lines/mm corresponding to a line spacing of about 0.8 μm. While scattering may limit the resolution accessible in a porous glass matrix and therefore the grating's dispersion, gratings created by photodeposition in a porous glass and then consolidated to a nonporous glass possess a thermal stability unmatched by gratings produced by any other technique, or in any other medium, including conventional grooved gratings. Consolidation improves optical performance by decreasing line spacing and increasing dispersion, but it also encapsulates the grating within the glass. As the SiO_2 nodules broaden and meld together at higher temperature, a 5-nm-thick layer of glass forms over the photodeposited image thereby protecting it from the surroundings.[13,99] Isolated from the exterior environment by this 5-nm layer of glass, the encapsulated grating are unaffected by oxidizing or reducing atmospheres, organic solvents, and UV and high incident laser powers.[99]

While accessible resolution and, therefore, grating dispersion are independent of the deposition technique, optical performance depends on the deposition method. Specifically, the holographically deposited gratings yield a larger number of diffraction orders with higher relative intensities and more symmetric intensity profiles than those obtained with gratings created by either photolithography or laser writing. Typically, four to five diffraction orders are visible with the holographic gratings, whereas those prepared by the other procedures failed to show more than one or two higher orders. The intensity profiles of each diffraction order obtained with holographic gratings parallel that of the fundamental, and the relative intensity of the first-order maxima are typically 45–50% of the fundamental, whereas the first-order maxima with an equivalent laser-written grating is $\leq 10\%$ the intensity of the fundamental.[97–99] With gratings consisting of 5-μm-wide lines spaced about 10 μm apart, the relative intensities of the maxima observed with the holographic grating are four to five times those obtained from the photolithographic or laser-written gratings.[99] Also, the holographic gratings failed to show the ghost images found with the laser-written gratings.[99]

Photodeposition in porous glass has yet to achieve number of lines/mm available in scribed gratings, but is readily adaptable to creating gratings or optical components in unique places. For example, Bragg gratings have been created holographically and by laser writing on the side of a 180-μm diameter optical fiber composed of a solid 80–100-μm diameter core with a 40–50-μm-thick porous cladding. The porous cladding was impregnated with $Fe(CO)_5$ and the regions of higher refractive index created by moving the impregnated fiber across the focused 488-nm laser beam. The regions of higher refractive index, which contain iron oxide with no evidence of elemental iron, appear as parallel lines across the width of the fiber (Figure 31). Because of the curved surface of the fiber, however, the resolution defined by the micropositioner and the focus of the excitation exists only along a line on the fiber surface parallel to the fiber axis. Consequently, resolution declines as the surface,

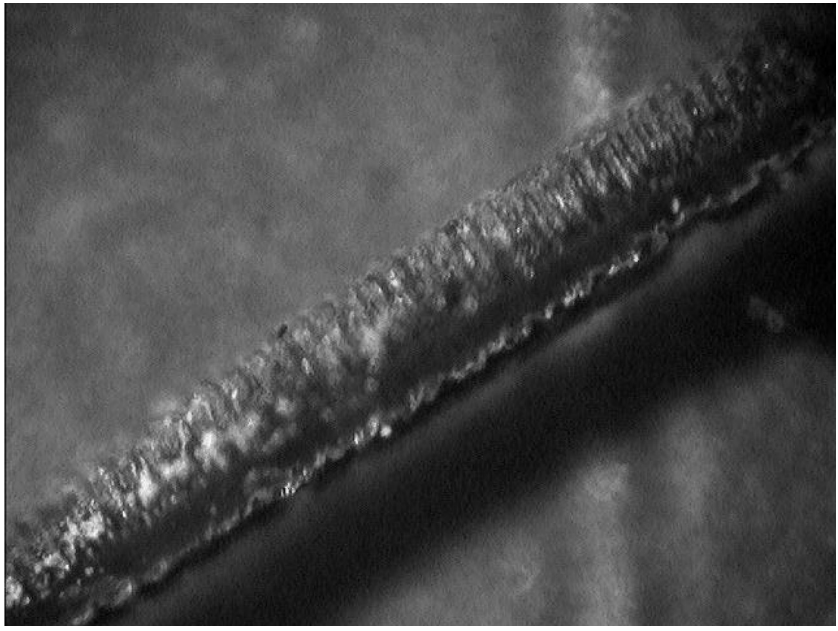

FIGURE 31 Bragg grating photodeposited in the cladding of a 180-μm diameter optical fiber.

because of its curvature, either moves closer to, or away from the focal point of the excitation. Nevertheless, optical micrographs (Figure 31) reveal well-defined, 4 ± 1-μm-wide, parallel regions of higher refractive index separated by 6 ± 1-μm-wide, undoped regions on the side of the fiber. Although the line width is slightly smaller than that found in PVG, where resolution declines at dimensions below 5 μm, deposition in the porous cladding of the fiber was expected to be similar to that in PVG, where photodeposition creates the grating within the PVG matrix and consolidation encapsulates the image under a 5-nm layer of SiO_2. After heating the fiber to 600°C, however, atomic force microscopy (Figure 32) reveals that the grating consists of 2–4-μm-high ridges on the cladding surface. In fact, the grating produced on the fiber resembles a conventional grooved grating, where the regions containing the photodeposited iron oxide appear as raised ridges and the unexposed regions as intervening troughs. AFM also yields a somewhat larger line width, ca. 8–10 μm, but it is not clear whether this reflects the loss of focus due to the curvature of the fiber. In other words, it is not known whether the AFM is examining the grating along the focal line, or slightly off the focal line where the size of the excitation beam changes as a result of the curvature of the fiber, thereby reducing resolution. Furthermore, since the ridges shown

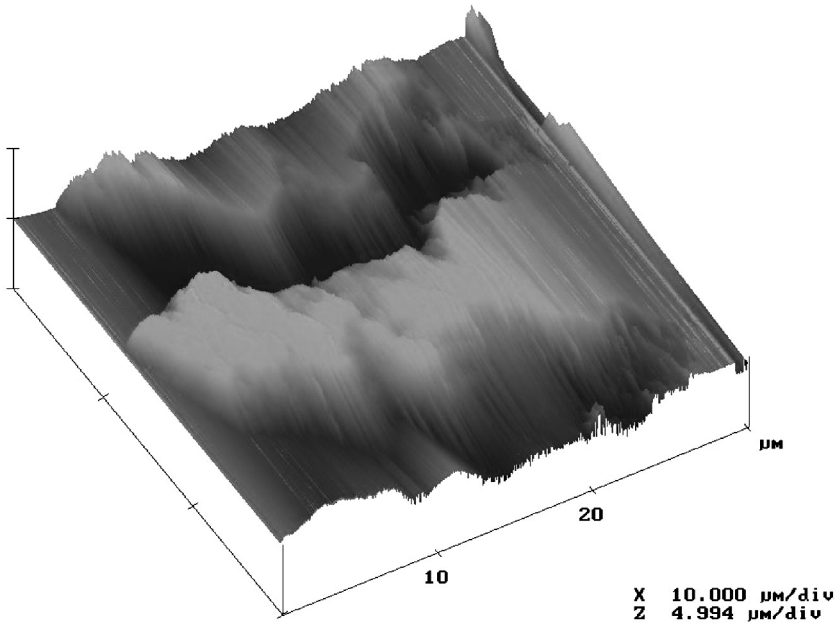

FIGURE 32 AFM of Bragg grating photodeposited on optical fiber with the lighter color indicating image height.

in Figure 32 are not observed on PVG, it is not clear whether the grating is on the surface of the fiber or extends into the cladding of the fiber analogous to those photodeposited in PVG. Measurements of the distribution of iron in PVG show that $Fe(CO)_5$ uniformly impregnates PVG to a depth of $\geq 1600\,\mu m$ (Figure 14).[13] Photolysis increases the amount of iron in the first 300 μm, and consolidation creates a 5-nm layer of essentially pure SiO_2 glass over a distribution of iron extending 200–300 μm into the glass. Since the cladding of these fibers is also porous, and these depths exceed the thickness of the cladding, 40–50 μm, it is quite possible that grating, i.e., the regions of differing optical density and refractive index, are not just limited to the outer surfaces, but extend into the cladding. Comparisons of the spatial distribution of the light transmitted through the fiber before and after deposition of the grating, however, indicate that photodeposition of the grating does not compromise the integrity of the core. Therefore, the grating shown in Figure 31 is either limited to the surface of the cladding or extends into the cladding, although at present the depth the grating extends into the cladding is not known.

Interest in establishing the position of the grating relative to the core arises from the surprising result that the grating can be used *to insert and remove light from the core of the fiber*. For example, no light emanates from the

end of the fiber when 632-nm laser light impinges onto the side of the fiber. When the light is directed onto the photodeposited grating, however, 632-nm light emanates from the end of the fiber. Furthermore, light introduced into the fiber core at the end of the fiber is not scattered from the fiber except at the photodeposited grating. If the grating is placed at a bend in the fiber, the amount of light exiting the core becomes a function of the bend in the fiber, and can be varied by small movements of the fiber. Initial measurements yield a coupling efficiency, i.e., the ratio of power emanating from the end of the fiber relative to the power incident on the grating, of $\leq 1\%$, but this is a lower limit uncorrected for scattering loses at the air-grating interface or transmission losses through the fiber. Nevertheless, the results establish proof of concept and show that a grating photodeposited into the cladding of the fiber can be used to introduce and remove light from the fiber core without compromising the integrity of the core.

Active Optical Structures

All optical networks consist of active and passive elements with the passive elements guiding the light to active elements that modulate the frequency, phase, or coherence of the photons passing through the device. While the above demonstrates feasibility with respect to creating passive structures via photodeposition in porous glass, the incorporation of active materials into these optical networks and addressing these materials either electrically, magnetically, or optically is equally important.[2,100,101] The ability to retain porosity in an otherwise consolidated glass, as discovered in the photodeposition of tin in PVG,[40] allows porous regions to be patterned in the glass that can be impregnated with different optical reagents.

An alternative approach is to transfer established technologies to porous glass. One of these, which is widely used to assemble electro-optic devices, is the use of glass coated with highly transparent, electrically conductive, indium-tin oxide, called ITO or Nesa glass.[102–107] Attempts to deposit conductive ITO coatings on porous glasses, however, led to loss of porosity as the metal aggregated in the pores.[47] This not only reduces the porosity and surface area of PVG, but also dramatically increased scattering, thereby reducing transmissivity. A procedure developed in this laboratory, however, patterns electrically conductive, transparent ITO films on PVG without a significant reduction in surface area of the glass or its porosity.[108] An Sn/In film with an atomic ratio, 0.08, cast onto PVG and heated to 650°C, for example, has a surface area of $158 \pm 10\,m^2/g$, which is only slightly less than the surface area of the underlying PVG, $184 \pm 10\,m^2/g$.[108] SEM suggests the ITO coating extends ca. 3 μm into the pore structure of the glass. Since this occurs with little change in surface area, to a first approximation, the morphology of the coated glass is similar to that of the uncoated glass. Furthermore, when the pore structure is filled with an electro-optic material, the depth of the conductive film into the pore structure of the glass creates a

path length, albeit short, but nevertheless much longer than that accessible in structures assembled by layering the reagent onto the ITO film on a nonporous glass. In the latter case, the voltage drop, and therefore the effective optical path length of the electro-optic effect, is limited to a few monolayers of the active reagent on the ITO surface. The electro-optic effect achieved in a PVG sample appears to extend much further through the sample. Figure 33 shows the spectral changes achieved in a PVG sample with ITO coated onto each face of the glass and impregnated with electro-optic reagent DR-1, 4-[N-(2-hydroxyethyl)-N-ethyl]-amino-4′-nitrobenzene. The application of 1.5 kV through the contacts attached to each ITO-coated face shifts the broad absorption of DR-1 to longer wavelength and reduces the absorption in the 375–525-nm region (Figure 33). The spectral changes are similar to the response

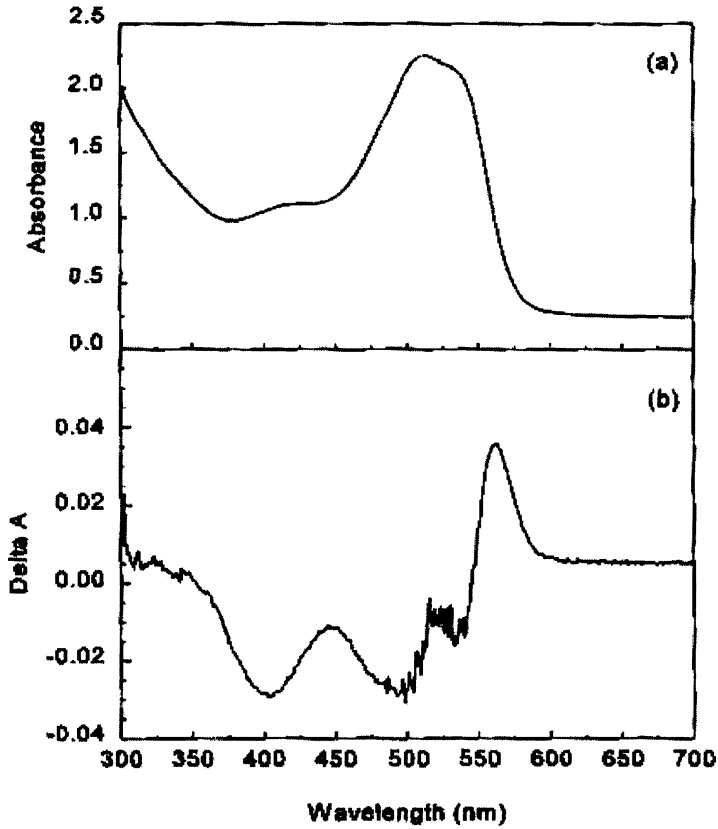

FIGURE 33 (a) Absorption spectrum of DR-1 adsorbed onto ITO-coated PVG, and (b) the difference spectrum after the application of 1.5 kV.

achieved during corona poling a DR-1–doped polymer film with an applied voltage of 4 kV. In the later case, the spectral changes are attributed to a field-induced molecular ordering of the dye.[109] The similarity of the spectral changes in PVG suggests a similar ordering within the pores of the glass with the application of a field. The spectral change is reversible when the electric field is shut off, although the recovery is slow in PVG, requiring a couple of hours to recover ca. 90% of the initial spectrum.

The electrical and optical properties of the films depend on the tin:indium ratio (Figure 34) and the annealing temperature (Figure 35). Decomposition of the In and Sn precursors occurs at 560°C and heating an Sn/In film with a 0.08 atomic ratio to 600°C reduces its resistance to 1 kΩ/square. The

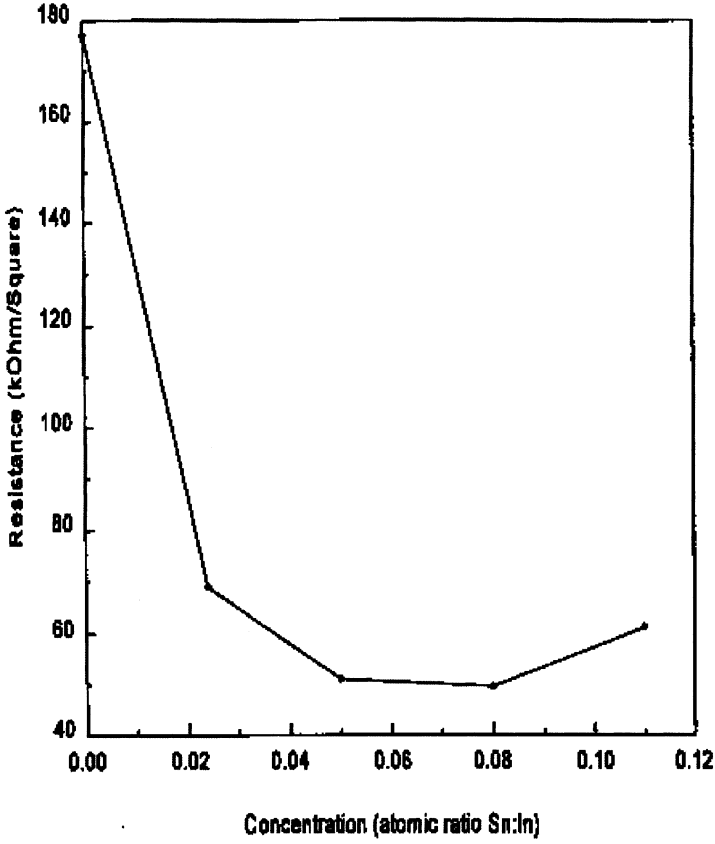

FIGURE 34 Variation of the resistance of the ITO coating on PVG as a function of the Sn:In ratio.

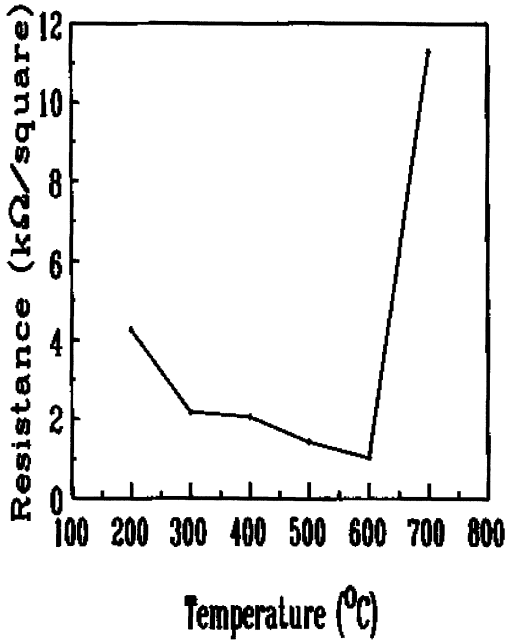

FIGURE 35 Variation of ITO resistance as a function of annealing temperature. 0.08 Sn:In ratio.

reduction in resistance occurs with a concurrent crystallization of the ITO (Figure 36), yielding a coating composed of ca. 20-nm diameter particles. Dispersed on the SiO_2 nodules, the coated sample retains the morphology of the underlying PVG (Figure 1) with the film reducing the surface area by no more than 14%. Although the ITO appears to be composed of 20-nm diameter crystals, these crystals are in electrical contact so that the film is electrically conductive with a resistance of 0.1 Ω/cm. The resistivity of films cast on PVG is larger than ITO films cast on nonporous glass, yet the resistance and optical transparency of the coated porous glass are sufficient for many practical applications. In the 400 to 1200 nm region, for example, the coated glass retains an optical transmittance of 85% relative to untreated PVG (Figure 37). The absorptions at 1400 and 1900 nm, which are present in the spectrum of PVG and the coated samples, are overtones of the intense SiO-H vibrations of the free and associated silanols.[47] The appearance of overtone vibrations in the coated samples suggests incomplete coverage of the PVG by the ITO films. However, non-uniformities are not apparent in the ITO films and are not detectable in samples impregnated with DR-1.

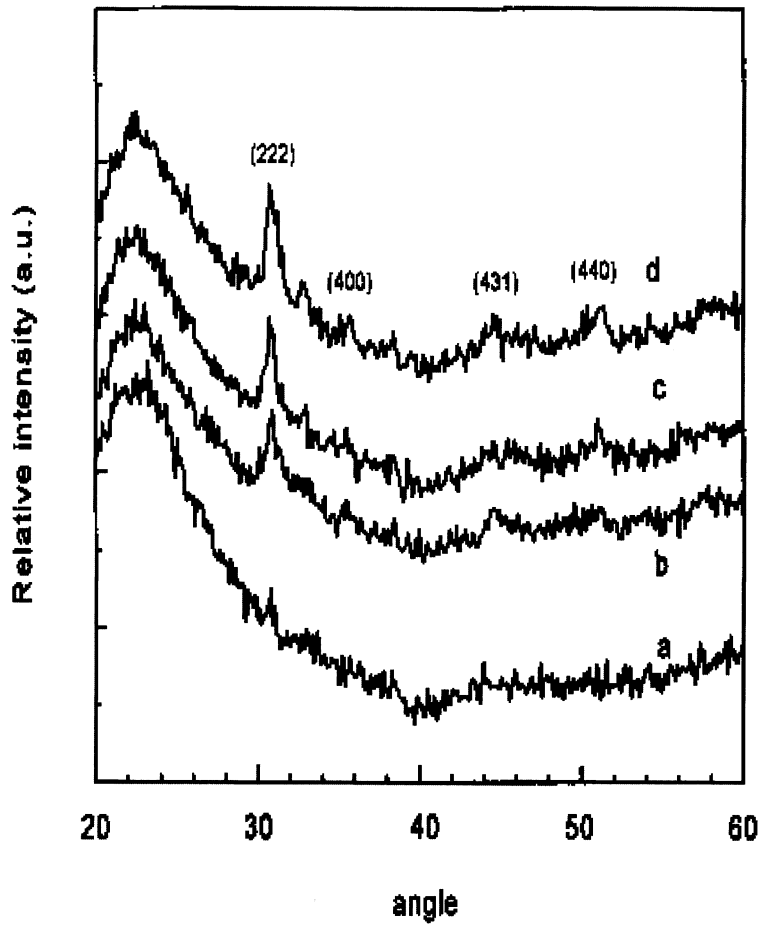

FIGURE 36 X-ray diffraction patterns of ITO coated on PVG after heating to (a) 300°C, (b) 400°C, (c) 500°C, and (d) 600°C.

The spectral changes obtained when 1.5 kV is applied to the sample containing DR-1 appear very uniform across each face of the sample, and spectra recorded at different locations on the sample agree within experimental error, suggesting that the ITO films deposited on PVG, at least from the optical applications point of view, are relatively uniform. Since the ITO extends ca. 10 μm into the pore structure, the overtones are attributed to the uncoated interior portions of the glass. The ITO cast onto PVG can also be patterned (Figure 38) currently with a resolution on the order of 50 μm.[47]

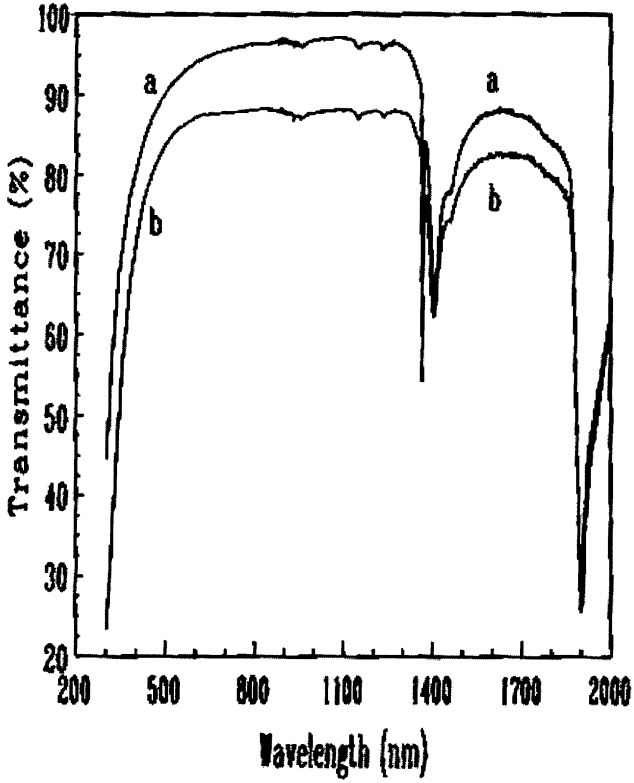

FIGURE 37 Transparency relative to air of (a) PVG and (b) ITO-coated PVG.

SUMMARY

Photodeposition of metals and/or metal oxides in porous glass and porous xerogels followed by thermal consolidation to a nonporous glass is a promising approach to integrated optics in glass. As illustrated, passive structures that, depending on shape, guide, focus and defract light. Nevertheless, a number of fundamental questions must be resolved to optimize optical performance. Δn, for example, is a function of the change in the density and polarizability (Eq. 2) induced by the deposition of the metal and/or metal oxide. However, it is not clear whether Δn achieved depends equally on both, or predominantly on one or the other. Is it better to use a precursor that produces the largest density change, or one that produces the largest change in polarization, or both? The metals described in this summary were

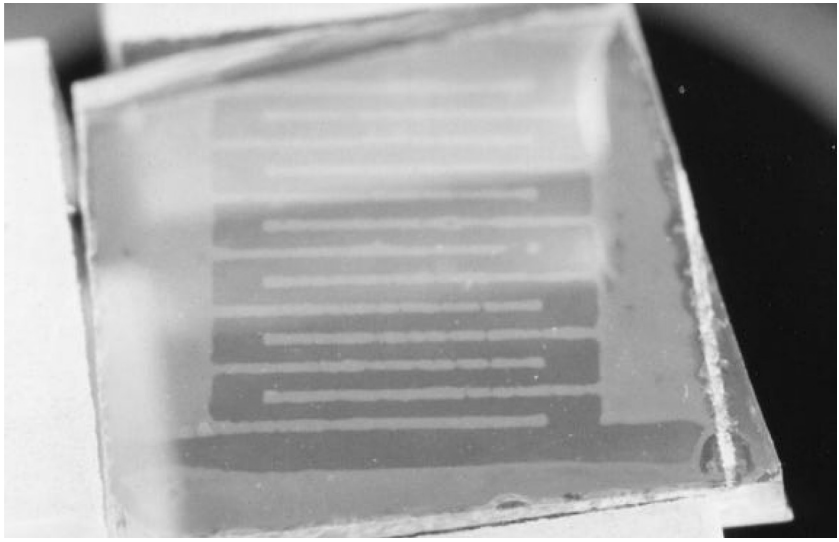

FIGURE 38 ITO pattern on PVG. Width of the horizontal ITO lines is ca. 100 μm.

chosen for their photochemical activity, volatility, band gap, or behavior in SiO_2 matrices with no consideration of either product density or polarizability. Other metals, including Ti and Pb, have been examined and, although each produces a change in refractive index, each is subject to foibles that either limit use or optical performance of the photodeposited structure. Hence, a rich, wide experimental vista exists in which to correlate photodeposition and optical performance of the deposited material.

Regardless of the specific precursor, the changes in refractive index described above were achieved with relatively low precursor loadings, $\leq 10^{-4}$ mol/g, suggesting that deposition does not significantly change the density of the glass. It must be noted, however, that diffusion of both iron and tin within the glass during photolysis challenges this assumption. Nevertheless, at this point, the low precursor loadings used suggest the changes in refractive index arise principally from a change in the polarizability of the volume of glass containing the metal and/metal oxide. Equation 2 refers to isotropic, homogeneous media, yet the gradient indices produced with iron, whether due to a change in density, polarizability, or both, are neither homogeneous nor isotropic. Rather, they consist of a distribution of 10 ± 1-nm diameter particles with an average spacing of 22 ± 1 nm. Can this be treated as an average since the size of the particles and their average spacing is less than the wavelength of the visible or near-IR light transmitted through the gradient index structure?

The various structures created by the photodeposition of metals and metal oxides possess high transparency ($\geq 85\%$ vs. air) in the 1300–1500-nm region, where optical transmission is expected to occur. Nevertheless, transparency at shorter wavelengths is desirable to provide the widest experimental latitude in devising structures capable of modifying the frequency, phase, and/or coherence of photons passing through the circuit. Beyond the band gap of the metal or metal oxide used to achieve a refractive index change, however, it is not clear what controls the transparency of these nanometer diameter particles in these SiO_2 matrices. The correlation between Fe-Fe_2O_3 particle size and the onset of absorption found in PVG, attributed to a "quantum dot" effect, fails to extend to nearly identical spectral changes found in the xerogels, where particle growth does not occur during the subsequent heating and consolidation. The iron oxide, principally Fe_2O_3, is ≤ 1-nm in diameter after photolysis and remains ≤ 1-nm in diameter in the consolidated xerogel, although 50%T shifts to the red. Further work is needed to understand what controls not only the transparency, but also the physical properties of metal and metal oxide particles formed in porous matrices and in the consolidated glasses. At least with iron in these matrices, the magnetic properties correlate with particle size, but the optical properties do not.

Whether porous glasses and/or xerogels satisfy all the criteria of an "optical silicon" remains to be established, but the photodeposition of metal and metal oxides in glass, particularly in regard to the development of integrated optics, offers a wide experimental vista and new challenges for inorganic chemists. Merging the advances occurring in nanotechnology with the porosity and transparency of these materials, the ability to pattern transparent, electrically conductive coatings, and the ability to retain porosity within an otherwise consolidated optical network will dramatically increase the ability to innovate complex circuitry. Glass-based hybrids incorporating materials that respond to optical, electric, and magnetic stimuli not only provide routes to specific devices, but fundamental insights into the physical and chemical properties of nanometer metal and/or metal oxide particles in inorganic oxide matrices.

ACKNOWLEDGEMENT

Support of this research over the years by the National Science Foundation, the Office of Naval Research, the Air Force Office of Scientific Research, Petroleum Research Foundation, the City University of New York Center of Advance Technology in Ultrafast Photonics and Photonic Materials supported by the New York State Science and Technology Foundation, and the PSC-BHE Research Grants Program of the City University of New York, is gratefully acknowledged. Dr. Devi thanks the Indian Central Glass and Ceramic Research Institute for a leave of absence while working on these experiments.

REFERENCES

1. Miller, S. E. 1969. *Bell System Technical Journal* 48, 2059; 48, 2162.
2. Anderson, D. B. 1965. *Optical and Electro-Optical Information Processes*, Cambridge, MA: MIT Press, p. 221.
3. Glass, A. M. 1988. *Mater. Res. Soc.* XII(8), 14.
4. Vogel, E. M. 1989. *J. Am. Ceram. Soc.* 72(5), 719.
5. Smith, P. W. 1988. *Photonic Switching: Present Research and Future Propects, Optical Computing and Nonlinear Materials*, SPIE International Society for Optical Engineering, Bellingham, Wa., Vol. 881, p. 30.
6. 1987. Research on nonlinear optical materials: an assessment. *Appl. Optics* 26(2), 211.
7. Verber, C. M. 1984. *IEEE Proceedings* 72, 942.
8. Eaton, D. F. 1991. *Science* 253, 281.
9. Gafney, H. D. 1991. *J. Macromol. Sci.* 253, 281.
10. Wolkow, E., Mendoza, E., Hanson, A. L., Wong, P., Gafney, H. D. 1990. *Mater. Res. Soc. Symp.* 168, 381.
11. Gafney, H. D., Mendoza, E. A., Morse, D. L., 1991. *Proc. SPIE-Int. Soc. Opt. Eng.* 1583, 43.
12. Gafney, H. D., Mendoza, E. A. 1992. The photochemical deposition of non-linear optical materials into porous glass, in *Nonlinear Optical Materials*, H. Kuhn, J. Robillard, eds. London: CRC Press, p. 179.
13. Gafney, H. D. 1997. A photochemical approach to integrated optics, in *Chemistry in Industry*, D. Perry, ed. New York: Plenum Press, p. 189.
14. Gafney, H. D. 1989. *J. Imaging Science* 33, 37.
15. Sunil, D., Rafailovich, M., Sokolov, J., Gafney, H. D. 1995. *Inorganic Chemistry in Integrated Optics*, Second Nassau Mossbauer Conference, C. I. Wynter, E. E. Alp, ed., DuBuque, IA: W. C. Brown, p. 145.
16. Wolkow, E., Mendoza, E., Hanson, A. L., Sunil, D., Sokolov, J., Rafailovich, M., Long, G. G., Gafney, H. D. 1990. *Mater. Res. Soc. Symp.* 168, 387.
17. Brinker, C. J., Scherer, G. W. 1990. *Sol-Gel Science The Physics and Chemistry of Sol-Gel Processing*, San Diego, CA: Academic Press, p. 515.
18. Wolkow, E., Mendoza, E., Rafailovich, M., Sokolov, J., Hanson, A., Wilkins, B. J., DenBoer, M. L., Gafney, H. D., 1991. *Mater. Res. Soc. Symp.* 169, 191.
19. Gafney, H. D. 1989. *J. Imaging Science* 33, 37.
20. Young, M. 1986. *Optics and Lasers*, New York: Springer-Verlag, 3rd ed., p. 218.
21. Morgan, J. 1953. *Introduction to Geometric and Physical Optics*, New York: McGraw-Hill, pp. 223–227.
22. Robertson, J. K. 1954. *Introduction to Optics: Geometrical and Physical*, 4th ed., New York: Van Norstrand, p. 178.
23. Klein, M. V., Furtek, T. E. 1986. *Optics*, 2nd ed., New York: Wiley, p. 83.
24. Safford, E. L. 1984. *The Fiber Optics and Laser Handbook*, Blue Ridge Summit, PA: Tab, Ch. 1.
25. Sanchita, H., Dipankar, D. 1994. *J. Phys. Chem.* 98, 10451.
26. Arndt, J., Hummel, W. 1988. *Phys. Chem. Minerals* 15, 363.
27. Borrelli, N. F., Morse, D. L. 1983. *J. Appl. Phys.* 43, 992.
28. Borrelli, N. F., Morse, D. L., Seheurs, J. H. 1983. *J. Appl. Phys.* 54, 3344.
29. Borrelli, N. F., Morse, D. L. U. S. Pat. No. 4403031.
30. Wolkow, E., Mendoza, E., Hanson, A. L., Wong, P., Gafney, H. D. 1990. *Mater. Res. Soc. Symp.* 168, 381.

31. Gradient indices created with $Fe(CO)_5$ in PVG and Δn measured at 632 nm by the fringe displacement method.
32. Mendoza, E. A., Wolkow, E., Sunil, D., Sokolov, J., Rafailovich, M. H., Gafney, H. D. 1991. *Langmuir* 7, 3046.
33. Darsillo, M. S., Paquette, M., Gafney, H. D. 1987. *J. Am. Chem. Soc.* 109, 3275.
34. Sunil, D., Rafailovich, M., Sokolov, J., Gafney, H. D. 1993. *Inorg. Chem.* 32, 4489.
35. Dong, J., Devi, S., Mendoza, E. A., Gafney, H. D. 2001. *Inorg. Chem.* 41, 11.
36. Sunil, D., Rafailovich, M., Sokolov, J., Kotyuhanski, B., Wilkins, B. J., Hanson, A. L., Gafney, H. D. 1993. *J. Appl. Phys.* 74, 3768.
37. Sunil, D., Rafailovich, M., Sokolov, J., Gambino, R. J., Tsang, C., Huang, D. M., Gafney, H. D. 1996. *J. Appl. Phys.* 79(8), 6025.
38. Mendoza, E. A,, Wolkow, E., Gafney, H. D., Sunil, D., Rafailovich, M., Sokolov, J., Long, G., Jemian, J. 1990. *J. Appl. Phys.* 57(10), 209.
39. Sunil, D., Rafailovich, M. H., Sokolov, J., Gambino, R. J., Huang, D. M., Gafney, H. D. 2003. *J. Non-Crystal. Solids* 319(1–2), 154.
40. Sunil, D., Dong, J., Schwarz, S. A., Gafney, H. D. 2003. *J. Non-Crystal. Solids* 319(1–2), 163.
41. Elmer, T. H., Chapman, I. D., Norberg, M. E. 1962. *J. Phys. Chem.* 66, 1517.
42. Iler, R. K. 1979. *The Chemistry of Silica*, New York: Wiley-Interscience, p. 551, 622–714.
43. Janowski, V. F., Heyer, W. 1989. *Z. Chem.* 19, 1.
44. Cant, N. W., Little, L. H. 1964. *Can. J. Chem.* 42, 802; 1965. 43, 1252.
45. Chapman, I. D., Hair, M. L. 1966. *J. Am. Cearm. Soc.* 49, 651.
46. Wiltzius, P., Bates, F. S., Dierker, S. B., Wignall, G. D. 1987. *Phys. Revs.* 36, 2991.
47. Dong, J. 1997. Ph.D. Thesis, City University of New York.
48. Sunil, D., Gafney, H. D. *J. Phys. Chem.* submitted.
49. Adamson, A. W. 1976. *Physical Chemistry of Surfaces*, New York: John Wiley, 3rd ed., p. 616.
50. Jesson, J. P., Muetterties, E. L. 1969. *Basic Chemical and Physical Data*. New York: Marcel Dekker, p. 16.
51. Snyder, L. R., Ward, J. W. 1966. *J. Phys. Chem.* 70, 3941.
52. Simon, R. C., Mendoza, E., Gafney, H. D. 1988. *Inorg. Chem.* 27, 2733.
53. Gafney, H. D. Photochemistry of metal carbonyls physisorbed on porous Vycor glass. *Photochemistry on Solid Surfaces*, T. Matsuura, M. Anpo, ed. Amsterdam: Elsevier, 272.
54. Scholz, H. 1991. *Glass: Nature, Structure and Properties*, New York: Springer, p. 192.
55. Yukawa, Y. 1965. *Handbook of Organic Structural Analysis*. New York: Benjamin, pp. 544–545.
56. Bigorgne, M. 1970. *Organomet. Chem.* 24, 211.
57. Fan, J., Gafney, H. D. 1994. *J. Phys. Chem.* 98, 13058.
58. Shi, W., Gafney, H. D. 1987. *J. Am. Chem. Soc.* 109, 1582.
59. Devi, S., Petricevic, V., Alfano, R. R., Gafney, H. D. 1996. *J. Non-Crystal. Solids* 203, 78.
60. Devi, S., Petricevic, V., Alfano, R. R., He, D., Miyano, K. E., Gafney, H. D. 2000. *Chem. Mater.* 12, 1378.
61. El-Sayed, M. A. 2001. *Acc. Chem. Res.* 34, 257.
62. Brust, M., Kiely, C. J. 2002. *Colloids & Surfaces* A202, 175.
63. Bonnemann, H., Richards, R. M. 2001. *Eur. J. Inorg. Chem.* 2455.
64. Pham, M. T., Moller, D., Matz, W., Mucklich, A., Oswald, S. 1998. *J. Phys. Chem. B* 102, 4081.
65. Bruhwiler, D., Seifert, R., Calzaferri, G. 1998. *J. Phys. Chem. B* 103, 6397.
66. Ptatschek, V. *et al.* 1997. *J. Phys. Chem. B* 101, 8898.

67. Linderoth, S., Morup, S., Bentzon, M. D. 1995. *J. Mat. Sci.* 30, 3142.
68. Sunil, D., Rafailovich, M., Sokolov, J., Gambino, R. J., Tsang, C., Huang, D. M. 1996. *J. Appl. Phys.* 79(8), 6025.
69. Dorman, J. L., Gibart, P., Suran, G., Sella, C. 1977. *Physica* 86–88B, 1431.
70. Gangopadhyay, S., Hadjipanayis, G. C., Dale, B., Sorensen, C. M., Klabunde, K. J. 1998. *Phys. Rev. B* 45, 3768.
71. Xiao, G., Chien, C. L. 1988. *J. Appl. Phys.* 63, 4252.
72. Morrish, A. H. 1980. *The Physical Principals of Magnetism*. New York: Robert E. Krieger, p. 340.
73. Papaefthymiou, V., Kostikas, A., Simopoullous, A., Niarchos, S., Gangopadhyay, S., Hadjipanayis, G. C., Sorensen, C. M., Klabunde, K. J. 1990. *J. Appl. Phys.* 67, 4487.
74. Tykachinskii, I. D., Fedorovskii, Y. A., Dzhakhva, N. G., Ovchinnikov, A. I., Tsyganov, A. D. 1974. *Inorg. Mater.* 10, 1883.
75. Muller-Warmuth, W., Eckert, H. 1982. *Phys. Reports* 88(2), 91.
76. Fuluzumi, S., Kochi, J. K. 1980. *J. Phys. Chem.* 84, 617; *J. Org. Chem.* 42, 2654.
77. Mendoza, E. A., Gafney, H. D. 1990. *Inorg. Chem.* 29, 4853.
78. Sawyer, A. K. 1971. *Organotin Compounds*, New York: Marcel-Dekker, Vol. 1, p. 110.
79. Van der Berghe, E. V., Van der Kelen. 1969. *J. Organomet. Chem.* 11, 479; 1969. 16, 497.
80. Cotton, F. A., Wilkinson, G. 1988. *Advanced Inorganic Chemistry* 5th ed., New York: Wiley-Interscience, p. 292.
81. Bukshpan, S., Pattyn, H. 1991. *Chem. Phys. Lett.* 177(3), 269.
82. Ben Amor, N., Daniel, C. 2001. *Abstracts of the 14th International Symposium on the Photophysics and Photochemistry of Coordination Compounds*. Hungary: Veszprem, p. 66.
83. Lipson, M., Deniz, A. A., Peters, K. S. 1996. *J. Am. Chem. Soc.* 118, 2992.
84. Willemen, H. 1979. *Inorg. Chem. Acta.* 34, 175.
85. Kapani, N. S., Burke, J. J. 1972. *Optical Waveguides*. New York: Academic Press.
86. Marcusse, D. 1972. *Light Transmission Optics*. Princeton: Van Nostrand Reinhold.
87. Marcusse, D. 1973. *Integrated Optics*. New York: IEEE Press.
88. Synder, A. W., Love, J. D. 1983. *Optical Waveguide Theory*, New York: Chapman & Hall, p. 599.
89. Valette, S., Gidon, P., Jadot, J. P. 1987. *Proceedings 4th European Conference on Integrated Optics*, Scotland: Glasgow, p. 110.
90. Austin, D. H. 1987. *Appl. Opt.* 26(2), 211.
91. Borrelli, N. F., Cotter, M. D., Luong, J. C. 1986. *IEEE J. Quantum Electronics*, *QE-* 22(6), 896.
92. Gallorenzi, T. G. 1973. *Appl. Opt.* 12, 6.
93. Walker, R. G., Wilkinson, C. D. W. 1983. *Appl. Opt.* 22, 1929.
94. Mendoza, E. A., Gafney, H. D., Morse, D. L. 1991. *Proceeding SPIE-Int. Soc. Opt. Eng.* 1378, 139.
95. Mendoza, E. A., Gafney, H. D., Morse, D. L. 1991. *Proceeding SPIE-Int. Soc. Opt. Eng.* 1583, 43.
96. Mendoza, E. C. 1992. Ph.D. Thesis, City University of New York.
97. Gafney, H. D., Sunil, D., McQuade, A. W. 1998. *Appl. Spectrosc.* 52, 1014.
98. Gafney, H. D., McQuade, A. W., Sunil, D. 1999. *Proc. of SPIE* 3778, 139.
99. Gafney, H. D., McQuade, A. W., Sunil, D. 2000. *Appl. Spectrosc.* 54(6), 869.
100. Wilson, J., Hawkes, J. F. B. 1983. *Optoelectrotronics: An Introduction*. New York: Prentice Hall, Chapter 9.

101. Tsai, C. S. 1991. Optical modulation: Acousto-Optical devices in *Handbook of Microwave and Optical Components*, Vol. 4, Chang, K., ed., New York: John Wiley, p. 201.
102. Hamberg, I., Granqvist, C. G. 1986. *J. Appl. Phys.* 60(11), 123.
103. Adachi, K., Hirayama, T., Sakata, H. 1990. *J. Mater. Sci.* 25(28), 1403.
104. Yamamoto, O., Sasamoto, T., Inagaki, M. 1992. *J. Mater. Res.* 7(9), 2488.
105. Shigesato, Y., Hayashi, Y., Haranoh, T. 1992. *Appl. Phys. Lett.* 61(1), 73.
106. Gallagher, D., Scanlan, F., Houriet, R., Lausanne, F., Ring, T. A. 1993. *J. Mater. Res.* 8(12), 3135.
107. Mattox, D. M. 1991. *Thin Solid Films* 204, 25.
108. Gafney, H. D., Dong, J. 1996. *J. Non-Crystal. Solids* 203, 329.
109. Page, R. H., Jurich, M. C., Reck, B., Sen, A., Tweig, R. J., Swalan, J. D., Bjorklund, G. C., Willson, C. G. 1990. *J. Opt. Soc. Am.* B7, 1239.